DEPARTMENT OF PHYSICS
UNIVERSITY OF JYVÄSKYLÄ
JYFL RESEARCH REPORT 9/14

Spherically Symmetric Inhomogeneous Cosmological Models

BY
MIKKO PÄÄKKÖNEN

Academic Dissertation
for the Degree of
Doctor of Philosophy

Jyväskylä, Finland
September 2014

Preface

This thesis was crafted at the Department of Physics of the University of Jyväskylä during the years 2010-2014.

I would like to thank Prof. Kimmo Kainulainen for guidance and supervision over the course of this work. I'm in gratitude to Dr. Wessel Valkenburg for collaboration and especially to Dr. Valerio Marra for collaboration and guidance which have been of foundational importance. I also want to thank Dr. Syksy Räsänen and Dr. Troels Haugbølle for reviewing the manuscript and Dr. Tomi Koivisto for being my opponent. Finally I would like to express my deepest gratitude to Katri and the rest of my family for being there.

The financial support from the Magnus Ehrnrooth Foundation and the Helsinki Institute of Physics is gratefully acknowledged.

Mikko Pääkkönen

Jyväkylä, Summer 2014

List of Publications

This thesis consists of an introductory part and of the following publications:

I Observational Constraints on the ΛLTB model
Valerio Marra & Mikko Pääkkönen
JCAP **1012** (2010) 021 [arXiv:1009.4193 [astro-ph.CO]].

II Exact Spherically-Symmetric Inhomogeneous Model with n Perfect Fluids
Valerio Marra & Mikko Pääkkönen
JCAP **1201** (2012) 025 [arXiv:1105.6099 [gr-qc]].

III Bias on w from Large-Scale Structure
Valerio Marra, Mikko Pääkkönen & Wessel Valkenburg
Mon. Not. Roy. Astron. Soc. **431** (2013) 1891 [arXiv:1203.2180 [astro-ph.CO]].

The author has done all the calculations, the Mathematica code and writing of the manuscripts in publications [I-II] equally contributing together with the coauthor Dr. Valerio Marra. Publication [III] was based on a model and code developed in [I-II], and the author participated in writing the final form of the manuscript.

Abstract

Universe is statistically homogeneous and isotropic in our cosmic neighbourhood. In the standard model such universe is described with perfectly homogeneous and isotropic Friedmann-Lemaître-Robertson-Walker (FLRW) model. However, statistical homogeneity is not observationally established up to Gpc scales. This poses a problem: if the actual local spacetime geometry deviated from that of the FLRW model on cosmological scales, how would this affect our interpretation of observations?

In this thesis we employ spherically symmetric models in order to study the gravitational evolution of inhomogeneous coexisting perfect fluids. In particular, we study how a local large-scale inhomogeneity could alter our interpretation of cosmological observations.

A dust cosmology with a local underdensity can reproduce apparent acceleration on the luminosity distance-redshift relation fitting the supernovae type Ia observations. We study this so-called local-void scenario by doing likelihood analysis on models with both, a local void and a cosmological constant. It is found out that accommodating all the observations is difficult requiring a lot of fine tuning. We also find that a small local void would not alter the parameter extraction of the standard model. We also study models with a dark-energy component with vanishing speed of sound. In this case we find out that a local large-scale inhomogeneity of order $\delta_0 \approx 0.1$ in present-day dust density contrast, compatible with inflationary origin, could significantly alter our perception of dark energy equation of state. In conclusion we state that relaxing the prior of local homogeneity leads up to atleast 10% level uncertainties in cosmological parameter extraction.

Contents

1 Introduction

Cosmology differs from other physical sciences by its phenomenology fundamentally in that we, as observers, are confined to essentially one spacetime point to make observations on one specific system along past lightcone. We are clearly observing a physical system, but we have no control over the initial conditions through a preparation procedure. Moreover, we are not even able to make direct observations of the actual state of the whole system. In other words the nature of reality restricts us, when it comes to cosmology, from seeing nothing but a slice of the vast universe from one specific location at a one moment in time. Understanding such a setup naturally requires strong working hypothesis'.

One of the standard assumptions in modern cosmology is the so-called Copernican principle which states that the region of the universe we happen to inhabit does not possess cosmologically relevant peculiar features of any kind, so that the statistical features of the universe seen by us would be the same as those seen by an observer at any other randomly chosen place in the universe. Another standard assumption in cosmology is that the spatial distribution of the matter content of the universe possesses a high degree of statistical isotropy. This assumption is favoured by the observations of the cosmic microwave background radiation (CMB) [1] and the distribution of galaxies [2], [3]. If these two assumptions were true, it would then naturally follow that universe is also statistically homogeneous.

Stressing the idea of statistical homogeneity and isotropy, it is then assumed that the universe around us can be described essentially as a general relativistic homogeneous and isotropic perfect fluid with an associated homogeneous and isotropic Friedmann-Lemaître-Robertson-Walker (FLRW) metric. Although the present-day universe is clearly very far from exact homogeneity, the fact that the CMB temperature-fluctuation amplitudes are of order 10^{-5} suggests that matter was quite homogeneously distributed on the recombination surface. This then suggests that perhaps the exact metric of the universe converges towards a linearly perturbed FLRW metric at the early times. However, due to the non-linearity of general relativity, evolving the metric with an averaged source gives generally different results than solving for the full metric with an inhomogeneous source and then taking the average. The difference between the FLRW average of the evolved true metric and the evolved FLRW average is called backreaction.

In the current best-fit FLRW model, the concordance ΛCDM model, roughly 70% of the present-day energy density is attributed to the dark energy in the form of cosmological constant. By dark energy we mean a source of negative pressure on

cosmological scales. In the context of an FLRW model such pressure is required in order to accommodate that apparent acceleration observed on the type Ia supernovae magnitude-redshift relation. However, we do not have more profound knowledge about any fundamental physics to explain the dark energy, and the very small value of the cosmological constant invokes a fine-tuning problem; why the dark-energy dominance in the cosmic evolution has began only just lately in our cosmic past. However, the cosmological constant is only the simpliest way to accommodate the dark energy. Dark energy can also be modelled with effective dynamical fluids with negative pressure such as a dynamical scalar field (called quintessence) and such models have been studied in great detail [4]. Another approach is to generalize the Einstein-Hilbert action of general relativity, thus modifying the gravitational dynamics. The cosmological constant can be viewed also as such a generalization.

In addition to observations and theoretical considerations, numerical many-body simulations are used to study the evolution of large scale structures [5]. In N-body simulations one places a grid of mass points in an FLRW background and lets the mass points gravitate according to Newtonian gravity. However, In Newtonian gravity backreaction reduces to a boundary term which vanishes for boundary conditions applied in N-body simulations [6], [7]. Thus, N-body simulations neglect the backreaction. Indeed, in addition to invoking new physics (such as new fields or modified gravity) to solve the dark-energy problem, there are also more conservative lines of research trying to understand it in the context of backreaction. Some studies of the back reaction in a linearly perturbed FLRW metric, however, seem to imply that the effect on the Hubble rate due to the backreaction caused by linear contributions is negligible [8], [7].

It is, however, interesting to note that the statistical homogeneity in our cosmic neighborhood is not well established observationally up to gigaparsec scales [9], [10]. The type Ia supernovae luminosity distance-redshift relation could then in principle be reproduced in the context of locally inhomogeneous cosmological models. The interpretation of the measured cosmic observables then remain open to the possibility that the Copernican principle might not hold. Therefore, it seems tempting to try to explain the apparent acceleration rather with locally varying expansion rate than with a globally accelerating expansion rate. Such effect can be achieved in local-void models. These have been studied thoroughly recently, mostly in the context of spherically symmetric Lematre-Tolmann-Bondi (LTB) spacetimes [11, 12, 13, 14, 15, 16, 17, 18, 19, 20, 21, 22].

Even though the local-void scenario can accommodate the major observational features surprisingly well, it comes with serious difficulties. The local-void sce-

nario as an alternative to dark energy was studied in paper [I]. The results and difficulties mentioned are summarized in sections 5 and 6. However, apart from explaining away the need for dark energy we could still have a mixed scenario. Even if there is global acceleration due to some form of DE, the present state of observations can not prove the high degree of local homogeneity on Gpc scales assumed in the ΛCDM model. For this reason we can perfectly well ask how our intepretation of observations would change if we had a prior knowledge, say from future surveys, of such a local feature in the local matter distribution. Indeed, very large unvirialized structures are observed in the universe, such as large quasar groups (LQG's) possibly extending in length up to roughly one Gpc [26], [27], and hot and cold spots on the CMB which, if interpreted as of cosmological origin, would again correspond to structures up to a Gpc scale in diameter [29, 30, 31, 32].

In this thesis, assumption of spherical symmetry is used to compare void models of acceleration with the ΛCDM model and estimate uncertainties on cosmological parameters due to our ignorance of actual large-scale structure in our cosmic neighbourhood. Furthermore, the ADM formalism is employed to cast the equations of paper [II] in form with a wider numeric solvability and equations for setting appropriate initial conditions for more general models are presented. These results go beyond those contained in papers [I-III]. On the basis of likelihood analysis, the local-void explanation for dark energy does not seem to be a working alternative for cosmological constant. However, it turns out that dropping the prior of local homogeneity on large scales introduces significant uncertainties on our perception of dark energy. This was the main result of paper [III] for which we used a model developed in paper [II].

The thesis is organised as follows: section 2 introduces the principles of gravitational physics and their application to cosmology in the standard model. Section 3 summarizes the most important cosmic observables and the cosmological implications of their measurements. Section 4 consists of introduction of the spherically symmetric spacetimes and perfect-fluid sources, and of how to apply them in modelling local unvirialized inhomogeneous structures. In section 5, the cosmological applications studied in the papers [I-III] with their results are presented, and finally, section 6 is reserved for conclusions and discussion.

2 Gravitation and Cosmology

2.1 General Relativity

The present understanding of gravitational physics culminates in the theory of general relativity (GR) which is a classical, background independent field theory for gravity. In GR an idealized event is characterized by four numbers that will eventually correspond to the events position in the spacetime relative to other events. The multitude of all possible events is then thought to form a four dimensional spacetime continuum which is locally trivial, meaning that for each point on the continuum there exists a neighbourhood which can be mapped one-to-one on $\Re^4$. Such structure is called a differentiable manifold.

2.1.1 Spacetime Metric

In order to relate the points on the manifold to the physical distances between the corresponding events, the manifold is endowed with a metric structure. The metric structure is an inner product represented as a rank two covariant tensor, i.e. the metric tensor, usually denoted with $\mathrm{d}s^2$. The metric tensor then encodes the information of the gravitational field by determining the measurable spatio-temporal distances between possible events.

A coordinate system x^μ determines a basis on the cotangent (tangent) bundle by the exterior derivatives $\mathrm{d}x^\mu$ (partial derivative operators ∂_μ). In this basis one writes

$$\mathrm{d}s^2 = g_{\mu\nu}\mathrm{d}x^\mu\mathrm{d}x^\nu, \tag{2.1}$$

where the functions $g_{\mu\nu}$ are the components of the metric tensor in the coordinate basis and are postulated to be symmetric under exchange of indices μ and ν, thus leaving one with total of ten unknown functions. The metric tensors maps vectors into covectors forming the duality between tangent and cotangent spaces. The same applies to components of tensors so that in the coordinate basis the indices of tensor components can be raised and lowered by contracting with the inverse metric tensor and the metric tensor, respectively.

2.1.2 Covariant Derivative

The space-time manifold is given the Lorentzian signature $(-,+,+,+)$ dividing vectors into time-like, light-like and space-like types depending weather their amplitude squared is negative, null or positive, respectively, thus giving the manifold the causal structure of the space-time by making it locally Minkowskian. A vector in one Minkowskian tangent space is mapped into another by parallel transporting it along a curve joining the two points on the manifold. This procedure requires a covariant derivative operator ∇ which maps cotensors of rank k into cotensors of rank $k+1$. For a covector v the covariant derivative reads in the coordinate basis

$$\nabla_\mu v_\nu = \partial_\mu v_\nu + \Gamma^\xi{}_{\mu\nu} v_\xi, \tag{2.2}$$

where repeated index in contravariant and covariant positions is understood to be summed over and $\Gamma^\xi{}_{\mu\nu}$ is the affine connection coefficient. In GR it is taken to be the Christoffel connection, which is the unique torsionless and metric compatible connection i.e. it satisfies no torsion $\Gamma^\mu{}_{\nu\xi} - \Gamma^\mu{}_{\xi\nu} = 0$ and metric compatibility $\nabla_\mu g_{\nu\xi} = 0$ conditions. These two conditions determine the connection unambiguously. In the metric variables and coordinate basis we have

$$\Gamma^\mu{}_{\nu\xi} = \frac{1}{2} g^{\mu\rho} \left(g_{\nu\rho,\xi} + g_{\rho\xi,\nu} - g_{\nu\xi,\rho} \right), \tag{2.3}$$

where prime before an index denotes the partial derivative with respect to the corresponding coordinate.

Considering parallel transportation of the tangent vactor $\mathrm{d}x^\mu/\mathrm{d}\lambda$ of a curve $x^\mu(\lambda)$ gives the geodetic equation

$$\frac{\mathrm{d}^2 x^\mu}{\mathrm{d}\lambda} + \Gamma^\mu{}_{\nu\xi} \frac{\mathrm{d}x^\nu}{\mathrm{d}\lambda} \frac{\mathrm{d}x^\xi}{\mathrm{d}\lambda} = 0. \tag{2.4}$$

Solutions to this equation are called affine geodesics and in GR free particles, i.e. particles moving under the influence of gravity only, follow such geodesics. In fact the Christoffel connection is exactly the connection for which the geodesic equation is exactly the same as the Euler-Lagrange equation of motion for a free particle in curved background. Solutions to the latter being called metric geodesics.

2.1.3 Riemann Tensor

The curvature of a Riemannian manifold with no torsion is encoded in the Riemann tensor R which is a rank 4 tensor of $(1,3)$-type. It can be understood as the tensor determining local parallel transportation of a covector v around an infinitesimally small closed loop, giving a defining equation for the components in the coordinate basis

$$\nabla_\mu \nabla_\nu v_\xi - \nabla_\nu \nabla_\mu v_\xi = R_{\mu\nu\xi}{}^{\rho} v_\rho. \tag{2.5}$$

Written in terms of Christoffel connection this equation gives

$$R^{\mu}{}_{\nu\xi\rho} = \Gamma^{\mu}{}_{\rho\nu,\xi} - \Gamma^{\mu}{}_{\xi\nu,\rho} + \Gamma^{\mu}{}_{\xi\sigma}\Gamma^{\sigma}{}_{\rho\nu} - \Gamma^{\mu}{}_{\rho\sigma}\Gamma^{\sigma}{}_{\xi\nu}. \tag{2.6}$$

The Riemann tensor has the skew symmetry $R_{\mu\nu\xi\rho} = -R_{\nu\mu\xi\rho} = R_{\nu\mu\rho\xi}$ and the interchange symmetry $R_{\mu\nu\xi\rho} = R_{\xi\rho\mu\nu}$. Moreover, we define the Ricci tensor as the rank 2 covariant tensor formed from the Riemann tensor by the contraction $R_{\mu\nu} = R^{\xi}{}_{\mu\xi\nu}$, which is symmetric by the interchange symmetry, and the Ricci scalar by the double contraction $R = R^{\mu}{}_{\mu}$.

2.1.4 Einstein Equation

Gravity is sourced by the symmetric stress-energy tensor $T_{\mu\nu}$ dictated by the matter content and which satisfies the stress-energy-conservation law

$$\nabla^\nu T_{\nu\mu} = 0. \tag{2.7}$$

The metric of the manifold is then related to the matter content of the manifold by the Einstein equation

$$G_{\mu\nu} = \kappa T_{\mu\nu}, \tag{2.8}$$

where $G_{\mu\nu} \equiv R_{\mu\nu} - \frac{1}{2} g_{\mu\nu} R$ is the Einstein tensor, for which the conservation law $\nabla^\mu G_{\nu\mu} = 0$ manifestly holds (due to Bianchi identities), and $\kappa = 8\pi G$ is the Einstein's gravitational constant. From now on we adopt units for which $\kappa = 1$ and $c = 1$.

Einstein equation in vacuum can be obtained as Euler-Lagrange equation of motion with respect to metric from the Einstein-Hilbert action

$$S_{EH}[g_{\mu\nu}] = \int \mathrm{d}^4 x \sqrt{-g} R, \tag{2.9}$$

where g is the determinant of the metric tensor and R is the Ricci scalar. The energy-momentum-tensor part is obtained by including an action for the matter content.

Since the Einstein equation manifestly satisfies also the energy-momentum conservation equation, instead of ten, we actually have only six independent equations. This reflects the fact that we are dealing with a constrained system and four out of ten independent variables are actually unphysical gauge degrees of freedom.

2.1.5 ADM formalism

It is a remarkable fact that the covariant formulation of GR presented in the previous subsection does not give any preference for any particular choice of a time coordinate. However, direct applications require that the Einstein equation can be formulated as an initial value problem. In order to be able to cast the field equations of GR as a valid initial value problem, the Lorentzian space-time manifold needs to have the topology of $\Re \times \sigma$, where σ is a three dimensional compact Riemannian manifold without boundaries [33]. This implies that the solution manifold can always be understood as a one-parameter family of space-like hypersurfaces Σ_t called a foliation of the space-time, while the individual hypersurfaces are called leaves of foliation.

If we denote a coordinate patch on σ with coordinate labels x'^i, where $i = 1, 2, 3$, then we can find a time coordinate t' such that $x^\mu = (t', x'^i)$ forms a coordinate patch on the foliation $\Sigma_{t'}(\sigma)$. In these coordinates the metric tensor reads

$$\mathrm{d}s^2 = -\mathrm{d}t'^2 + h'_{ij}\mathrm{d}x'^i\mathrm{d}x'^j, \tag{2.10}$$

where $h'_{ij} = h'_{ij}(x'^\mu)$ is the induced metric on the three dimensional Riemannian manifolds formed by the embeddings $\Sigma_{t'}(\sigma)$. This special form restricts the reference frame to such that the coordinate time t' measures common proper time for all stationary observers. Due to the diffeomorphism invariance, however, we can always choose another coordinate system $x^\mu = x^\mu(x'^\nu)$ which takes the expression of Eq. (2.10) for the metric into

$$\mathrm{d}s^2 = -\alpha^2\mathrm{d}t^2 + h_{ij}\left(\mathrm{d}x^i + \beta^i\mathrm{d}t\right)\left(\mathrm{d}x^j + \beta^j\mathrm{d}t\right), \tag{2.11}$$

where functions $\alpha \equiv \left(\frac{\partial t'}{\partial t}\right)$ and $\beta^i \equiv h^{ij}\left(\frac{\partial t'}{\partial x^j}\right)\left(\frac{\partial t'}{\partial t}\right)$ are called the lapse and shift function, respectively. Thus, the metric can, without loss of generality, be

presented in the formally coordinatized form of Eq. (2.11), where the gauge degrees of freedom are readily separated into the lapse and shift functions by choosing a coordinate time t formally specifying the foliation. This form for the metric is called the ADM metric due to the Hamiltonian formulation of GR derived by Arnowitt, Deser and Misner using these specific variables [34].

The Hamiltonian formulation for GR can be achieved by starting from the Palatini action, which is just the Einstein-Hilbert action of Eq. (2.9), where however the connection coefficients are understood as independent variables. In this case the Christoffel connection is obtained as a solution to the equation of motion, and obtaining a Hamiltonian for h_{ij} and its canonically conjugate momenta π_{ij} can be done as in [34]. The same result can also be achieved by projecting the tensor calculus onto the spatial manifold with the metric h_{ij} as in [33].

The extrinsic curvature tensor, or the second fundamental form of the foliation, is defined as

$$2K_{\mu\nu} \equiv \left(\mathcal{L}_n \tilde{h}\right)_{\mu\nu} = \tilde{h}_\mu{}^\alpha \tilde{h}_\nu{}^\beta \nabla_{(\alpha} n_{\beta)}, \tag{2.12}$$

where $h_{\mu\nu} \equiv g_{\mu\nu} + n_\mu n_\nu$ is the projected metric on the leaves of foliation in four dimensions, which can be pulled back into h_{ij} of the spatial manifold. By projecting the extrinsic curvature on the spatial manifold one then obtains

$$K_{ij} \equiv \frac{1}{2\alpha}\left(-\dot{h}_{ij} + \mathcal{L}_\beta h_{ij}\right), \tag{2.13}$$

where dot denotes the partial derivative with respect to the time coordinate and $\mathcal{L}_\beta$ denotes the Lie derivative along the shift-vector field β^i. The extrinsic curvature (2.13) is related to the canonically conjugate momenta π_{ij} through [36]

$$\pi_{ij} = -\sqrt{h}\left(K_{ij} - h_{ij}K\right), \tag{2.14}$$

where h is the determinant of h_{ij} and K is the trace of the extrinsic curvature K_{ij}.

Equations of motion for these twelve independent variables become first order in time and read [37]:

$$\dot{h}_{ij} - \mathcal{L}_\beta h_{ij} = -2\alpha K_{ij}, \tag{2.15}$$

$$\dot{K}_{ij} - \mathcal{L}_\beta K_{ij} = -D_i D_j \alpha + \alpha\left(R_{ij} - 2K_{il}K^l{}_j + 2KK_{ij} - M_{ij}\right), \tag{2.16}$$

where D is the covariant derivative induced on the spatial manifolds and R_{ij} the corresponding Ricci tensor. The matter source term M_{ij} is defined in terms of

projections of the energy momentum tensor as

$$M_{ij} \equiv S_{ij} + \frac{1}{2} h_{ij} \left(\rho - S \right), \tag{2.17}$$

where

$$\rho \equiv n_\mu n_\nu T^{\mu\nu}, \tag{2.18}$$
$$S_i \equiv -h_{i\mu} n_\nu T^{\mu\nu}, \tag{2.19}$$
$$S_{ij} \equiv h_{i\mu} h_{j\nu} T^{\mu\nu}, \tag{2.20}$$

and $S = h^{ij} S_{ij}$ is the trace of S_{ij}. The covector n_μ is the time-like unit covector normal to the hypersurfaces Σ_t. Dynamic equations for variables h_{ij} in Eq. (2.16) follow from the definition of the extrinsic curvature of Eq. (2.12), while equations for the extrinsic curvature follow as Euler-Lagrange equations of motion for π_{ij} from the Lagrangian of the Palatini action written in terms of α, β^i, h_{ij} and π_{ij} [36]. There is no dependence on the time derivatives of α or β^i in the action so they can be interpreted as Lagrangian multipliers corresponding to constraints on phase space of the system. The equation of motion for α in particular gives the Hamiltonian constraint

$$\mathcal{H} \equiv 2\rho - R + K_{ij} K^{ij} - K^2 = 0, \tag{2.21}$$

which is the relativistic Hamiltonian of GR. Similarly the equation of motion for β^i gives the momentum-, or the diffeomorphism constraint:

$$S_i - D_j K^j{}_i + D_i K = 0. \tag{2.22}$$

The ADM equations (2.16) present the gravitational dynamics in linear, first-order form in the coordinate time, allowing a clear initial value formulation for a general gravitational system in principle. However, the numerical stability of ADM equations in this formulation is not always guaranteed. This problem along with a proposition for numerically better adjusted variables (BSSN variables), was discussed in Ref. [37]. In any case, the ADM variables turn out to be sufficiently stable for our purposes.

2.2 Homogeneity

2.2.1 FLRW model

The Friedman-Lemaître-Robertson-Walker model (FLRW) is the solution in GR for an exactly homogeneous and isotropic perfect fluid source. While homogene-

ity in GR clearly includes more than just the FLRW model, the latter has found the most extensive usage due to its application to cosmology. For this reason, it is sufficient to concentrate only on the FLRW model in relation to homogeneous models for purposes of this thesis. In coordinate basis, in lapseless and shiftless gauge and in spherical, co-moving coordinates the Robertson-Walker metric reads

$$\mathrm{d}s^2 = -\mathrm{d}t^2 + a(t)^2 \left(\frac{1}{1-kr^2}\mathrm{d}r^2 + r^2(\mathrm{d}\theta^2 + \sin^2\theta \mathrm{d}\phi^2) \right), \tag{2.23}$$

where $a(t)$ is the scale factor and $k = -1, 0, 1$ is the curvature of the homogeneous spatial slices. Thus, the FLRW model consists of a homogeneous and isotropic three-dimensional spatial manifold which is of either hyperbolic ($k = -1$), flat ($k = 0$) or elliptic ($k = 1$) geometry and on which the physical distances evolve with time coordinate according to the scale factor $a(t)$.

Matter content in the FLRW model is given by the perfect-fluid-energy-momentum tensor

$$T_{\mu\nu} = (\rho + p)u_\mu u_\nu + p g_{\mu\nu}, \tag{2.24}$$

where the energy and pressure densities ρ and p are functions of the time coordinate only and $u_\mu = (1, 0, 0, 0)$ is the four-velocity of the fluid. Actually, since the densities are perfectly isotropic and homogeneous, two simultanously existing fluid components don't develop relative velocities, so that the energy-momentum tensor of Eq. (2.24) can be understood as comprising of several perfect-fluid components i.e. just writing $\rho = \sum_i \rho_i$ and $p = \sum_i p_i$. Assuming equation of state $p = w\rho$, where w is a constant, the 0-component of the conservation equation (2.7) gives the continuity equation

$$\dot{\rho} = -3(1 + w)H\rho, \tag{2.25}$$

where $H = \dot{a}/a$ is the Hubble rate. The overdot denotes derivation with respect to t. This equation is solved by the scaling relation for ρ

$$\rho = \rho_0 \left(\frac{a}{a_0} \right)^{-3(1+w)}, \tag{2.26}$$

where the subscript 0 refers to evaluation at the value for the coordinate time t_0 corresponding to the present time. Continuity equation (2.25) is in fact satisfied for each individual component separately, also the scaling relation (2.26) is satisfied for each individual component.

For the Robertson-Walker metric of Eq. (2.23) and the energy-momentum tensor of Eq. (2.24) the Einstein equation (2.8) gives two independent equations

$$\left(\frac{\dot{a}}{a}\right)^2 = \frac{1}{3}\rho - \frac{k}{a^2}, \tag{2.27}$$

$$\frac{\ddot{a}}{a} = -\frac{1}{6}(\rho + 3p). \tag{2.28}$$

The first equation is called the Friedmann equation and the second is called the acceleration equation. One immediately observes that in order the FLRW model to have positively accelerated expansion one must have $w < -1/3$. Since the acceleration equation can be obtained by differentiating the Friedmann equation and using the continuity equation, only two out of Eq's (2.25), (2.27) and (2.28) are independent.

The cosmic redshift of light z, due to the expansion of the universe, emitted by a distant object and observed by an observer in an FLRW universe, is related to the scale factor as $a(z) = \frac{a_0}{1+z}$, where a_0 is the scale factor evaluated at the present epoch t_0. Then writing density ρ in units of critical density $\Omega = \frac{\rho}{\rho_{\rm cr}}$, where $\rho_{\rm cr} = 3H^2$, and using the scaling relation (2.26), the Friedmann equation (2.27) gives for the Hubble rate in an FLRW model with n decoupled perfect fluids with equations of state $p_i = w_i\rho_i$

$$H(z)^2 = H_0^2\left(\sum_{i=1}^{n}\Omega_i(1+z)^{3(1+w_i)} + \Omega_k(1+z)^2\right), \tag{2.29}$$

where Ω_i refers to the density of the i:th component evaluated at the present epoch t_0, and $\Omega_k = -\frac{k}{3a_0^2H_0^2}$.

Sometimes it is advantageous to rewrite the metric (2.23) in terms of the so-called conformal $\eta = \int \frac{dt}{a(t)}$ i.e. $\mathrm{d}\eta = \frac{1}{a(t)}\mathrm{d}t$. In the conformal form the flat FLRW metric becomes

$$\mathrm{d}s^2 = a(\eta)^2\left(-\mathrm{d}\eta^2 + \mathrm{d}\vec{x}^{\,2}\right), \tag{2.30}$$

where $\mathrm{d}\vec{x}^{\,2}$ denotes the metric tensor of a three-dimensional Euclidean space. By using the conformal time as the time coordinate, a flat FLRW metric thus becomes a Minkowski space where physical (proper) distances between spacetime points get stretched according to evolution of the scale factor $a(\eta)$.

2.2.2 Linear Perturbation Theory

When the actual metric can be considered to be close to the actual average metric, called the background metric, it is useful to decompose the metric tensor as $g_{\mu\nu} = \tilde{g}_{\mu\nu} + h_{\mu\nu}$, where $\tilde{g}_{\mu\nu}$ represents the metric tensor of the background spacetime and $h_{\mu\nu}$ the deviation from it. For example, a perturbed flat FLRW metric in conformal time coordinate (2.30) can be written, in the conformal Newtonian gauge, as [42]

$$\mathrm{d}s^2 = a^2(\eta)\left(-(1+2\Phi)\mathrm{d}\eta^2 - 2w_\alpha^\perp \mathrm{d}\eta \mathrm{d}x^\alpha + \left((1-2\psi)\delta_{ab} + h_{ab}^{\perp\perp}\right)\mathrm{d}x^a \mathrm{d}x^b\right), \tag{2.31}$$

where Φ, ψ, $w_\alpha^\perp$ and $h_{ab}^{\perp\perp}$ are functions of coordinates η and $\vec{x}$, and δ_{ab} denotes the cartesian components of the three-dimensional Euclidean metric. Functions Ψ and ψ are scalar perturbations while $w_\alpha^\perp$ and $h_{ab}^{\perp\perp}$ are vector and tensor perturbations, respectively, both containing two independent degrees of freedom.

Assuming that there are no anisotropic pressures sets $\psi = \Phi$. Furthermore, it turns out that vector and tensor perturbations decouple from the scalar perturbation in the linearized Einstein equation. Thus, for the evolution of scalar perturbations in presence of isotropic pressure, it is enough to consider the perturbed metric with just one scalar degree of freedom [42].

$$\mathrm{d}s^2 = a^2(\eta)\left(-(1+2\Phi)\mathrm{d}\eta^2 + (1-2\Phi)\delta_{ab}\mathrm{d}x^a\mathrm{d}x^b\right). \tag{2.32}$$

Linearized equations of motion for perturbed perfect fluid source with equation of state $p = w\rho$, where $w = c_s^2 \equiv \frac{\partial p}{\partial \rho}$ is the adiabatic sound speed squared, lead to the equation [42]

$$\Phi'' + \frac{6(1+w)}{1+3w}\frac{\Phi'}{\eta} - k^2 w\Phi = 0 \tag{2.33}$$

for the gravitational potential Φ, where k is the mode number and prime denotes a derivative with respect to η. Equation (2.33) shows (this can be more explicitly seen e.g. by making the change of variables $\eta \to x \equiv k\eta$) that perturbations of perfect fluids on scales much larger than the Hubble radius (for $k\eta \ll 1$ the first-order term dominates over the last term) remain frozen with constant amplitude, and perturbations on scales well within the Hubble radius (when $k\eta \gg 1$ i.e. when the last term dominates overt the first-order term) undergo damped oscillations due to the small-scale effects of pressure gradients. This produces acoustic waves propagating in the primordial baryonic plasma, which then produce the features (acoustic peaks) observed on the CMB anisotropy spectrum, as

well as on the large-scale galaxy distribution. When there are both radiation and dust are present in the plasma the growth of dust perturbations on sub-Hubble scales is suppressed into logarithmic during the radiation dominated phase, while they grow linearily during the matter domination [42]. This suppression is due to the acoustic oscillations in the radiation component dominating the dynamics of the gravitational potential.

2.2.3 Averaging and Backreaction

The standard model describes the evolution of the universe with an FLRW model, where the densities are understood as spatial averages over cosmological scales. This description poses a problem because even if the universe was very nearly isotropic and homogeneous after the big bang, the real universe is obviously far from perfect isotropy and homogeneity. Spatial average over a true inhomogeneous solution is in general different from a solution to equations constructed with prior assumption of perfect homogeneity and isotropy. Difference between these two on an observable is called backreaction [44], [45], [46].

Once the time slicing of the manifold is chosen one can define averages over different scales on the spatial manifolds. Such considerations lead, in the context of the back-reaction problem, to the Buchert scheme [43], which is a widely used formalism to adress the problem of backreaction for irrotational dust cosmologies. When this procedure is employed, new terms arise in the spatially averaged Raychaudhuri equation and Hamiltonian constraint [43]:

$$3\frac{\ddot{a}_{\mathcal{D}}}{a_{\mathcal{D}}} + \frac{1}{2}\rho_{\mathcal{D}} - \Lambda = \mathcal{Q}_{\mathcal{D}}, \tag{2.34}$$

$$3\left(\frac{\dot{a}_{\mathcal{D}}}{a_{\mathcal{D}}}\right)^2 - \rho_{\mathcal{D}} + \frac{1}{2}\langle\mathcal{R}\rangle_{\mathcal{D}} - \Lambda = -\frac{1}{2}\mathcal{Q}_{\mathcal{D}}. \tag{2.35}$$

Here the average scale factor $a_{\mathcal{D}}$ is defined as the cubic root of the volume $V_{\mathcal{D}}$ of the averaging spatial domain, i.e. $a_{\mathcal{D}} \equiv (V_{\mathcal{D}})^{\frac{1}{3}}$, while $\rho_{\mathcal{D}} \equiv M_{\mathcal{D}}/V_{\mathcal{D}}$ and $\langle\mathcal{R}\rangle_{\mathcal{D}}$ are the spatially averaged mass-energy density and spatially averaged spatial Ricci scalar, respectively. As before, Λ is the cosmological constant. Finally the backreaction term $\mathcal{Q}_{\mathcal{D}}$ is defined as:

$$\mathcal{Q}_{\mathcal{D}} \equiv \frac{2}{3}\langle(\theta - \langle\theta\rangle_{\mathcal{D}})^2\rangle_{\mathcal{D}} - 2\langle\sigma^2\rangle_{\mathcal{D}}, \tag{2.36}$$

where θ and σ are the expansion- and shear scalars, respectively. Expansion scalar is the trace $\theta = g^{\mu\nu}\theta_{\mu\nu}$ of the expansion tensor $\theta_{\mu\nu}$ defined in Eq. (4.35).

Shear scalar σ is defined in Eq. (A.17) of paper [II]. Equation (2.34) shows that a positive back-reaction term contributes to the acceleration equation in the same way as a cosmological constant.

The backreaction problem has been adressed in the context of the Buchert formalism for a linearily perturbed FLRW model with different gauge choices for example in [47], [7], [8]. These authors concluded that in irrotational dust models the linear contributions are not likely to produce appreciable backreaction. However, their arguments are not entirely convincing due to their omitting the nonlinear and possibly nonanalytic contributions.

Swiss-cheese models are exact dust solutions to Einstein equation where spherically symmetric patches (with LTB metric) are smoothly embedded in an FLRW background. Backreaction in swiss-cheese models was studied e.g. in [48, 49, 50, 51, 52]. It was found that for models with a flat FLRW background and typical LTB patches with compensated inhomogeneity profiles, the backreaction effects to the local expansion rate are negligible. However, one may argue that these models have negligible backreaction by construction, because of the compensating ridge included to match the spherical dust model with the exact FLRW background. It can then be argued that we do not know with certainty how the actual spacetime metric should be described to accomodate the effects from the observed large-scale structure. Quite interestingly a statistically isotropic and homogeneous swiss-cheese model with spherical dust holes was developed in Ref. [53] in which the backreaction was of the order of magnitude comparable to dark energy in ΛCDM. In this model the holes are formally modelled by the LTB metric, but the authors had relaxed the usual assumption of monotoniously growing angular-diameter distance as viewed from the center of the hole. Despite of being a toy model and not an attempt at accurately describe the actual universe, it suffices to produce an example of statistically isotropic and inhomogeneous model with backreaction large enough to account for apparent acceleration of observed proportions. Furthermore, it should also be noted that it is not clear how the actual large-scale geometry of the universe should be modelled in the first place.

2.3 Standard Model

The current standard model of cosmology, the concordance ΛCDM-model, applies the ideas of cold dark matter (CDM) and inflation in a linearly perturbed FLRW-model-framework. And indeed, a flat FLRW cosmology seems to fit various observations supringly well. However, the cosmic concordance in an FLRW

model also requires inclusion of a non-vanishing cosmological constant. This is a straightforward implication of the observed luminosity distance-redshift relation of type Ia supernovae, which shows apparent acceleration in the late-time expansion of the universe in the FLRW context. A solution to this is a new fluid component, dark energy (DE), with negative pressure dominating on cosmological scales [4].

2.3.1 Inflation

The isotropy of the CMB implies that the real universe was very close to an FLRW solution at the time of recombination. This is problematic, since the CMB sky consists of several patches that shouldn't have been in causal contact before the recombination. Secondly, universe seems to be nearly flat, i.e. $\Omega = 1$. This is suprising since small initial deviations from the critical density grow during normal expansion, and so universe had to be extremely close to critical density at early times.

These problems are solved in a scenario where the early universe undergoes a phase of exponential expansion called inflation [38]. During exponential expansion the physical distances grow faster than the causal horizon. Thus the entire CMB sky may have been in causal contact at early times, if the inflationary phase was sufficiently long. Furthermore, exponential expansion takes Ω towards unity regardles of its initial value. Thus, inflation explains why universe is nearly flat today. This can be seen from the scaling relation (2.26) which implies that inflation dilutes all other densities except that of the inflaton field itself. At the same time H is constant, so that inflaton field density is driven towards the critical density, leaving the universe nearly flat on scales of the observable universe.

Inflation provides a mechanism to generate perturbations in energy density which seed the present-day structure of the universe. This happens through quantum field fluctuations which are stretched beyond the causal horizon during the exponential expansion. Actual inflationary models typically include a scalar field whose potential drives the inflation. However, the classical inflaton field must evolve slowly during inflation, and hence inflation can be approximated with a de Sitter solution [39]. It is thus effectively sourced only by a cosmological constant. From the Friedmann equation (2.27) we then have

$$\left(\frac{\dot{a}}{a}\right)^2 = H^2 = \frac{\Lambda}{3}, \tag{2.37}$$

which implies that $a(t) = a_0 e^{\sqrt{\frac{\Lambda}{3}}t}$. Thus, we find the constant causal-horizon distance l_H we get

$$l_H = a_0 \int_0^{t_0} \frac{dt}{a} = \frac{1}{H}, \tag{2.38}$$

as discussed above. Thus the physical Hubble radius remains constant, while the exponential evolution of the scale factor pushes all physical scales beyond the causal horizon. Deep within the Hubble radius the fluctuations around the classical inflaton field trajectory behave as quantum fields, but as the physical size of the mode grows beyond the causal horizon, the modes freeze as classical fluctuations in the primordial fluctuation spectrum, distributed in a scale invariant manner, i.e. producing the self-similar Harrison-Zel'dovich spectrum. See e.g [39] for details. This primordial spectrum then sets the initial conditions for structure formation and acoustic oscillations in the baryon-photon plasma.

The observationally interesting quantity, often used to describe the fluctuations quantitatively is the power spectrum $\mathcal{P}(k)$, or the variance of the Fourier mode δ_k of fluctuations $\delta \equiv \frac{\rho - \rho_0}{\rho_0}$ at scale k i.e.

$$\mathcal{P}(k) = \langle |\delta_k|^2 \rangle, \tag{2.39}$$

where $\langle ... \rangle$ denotes taking a quantum ensemble average.

The simpliest inflation models predict a gaussian distribution of scalar fluctuations with a power law spectrum i.e. $\mathcal{P}_f(k) \propto k^{n_s - 1}$, where n_s is the spectral index and k the Fourier mode. When $n_s = 1$ the power spectrum is scale invariant and thus the fluctuation amplitudes on different scales are drawn from the same Gaussian distribution. The fluctuation spectrum of the CMB is indeed observed to be nearly scale invariant, with $n_s = 0.9675$, and Gaussian with high accuracy [1]. As the fluctuations on different scales are of similar amplitudes and larger scales fell back into the causal horizon later in the cosmic evolution, the large scale fluctuations have had less time to evolve inside horizon. Together with the dust-like nature of the cold dark matter these features indicate a "bottom-up" hierarchy of structure formation, where small structures form first. This prediction is backed up by both observations and N-body simulations [78]. For this reason the standard inflationary paradigm poses a problem for the local-supervoid explanation for the dark energy: practically all fluctuations on adequate scales should be deep within the linear regime.

Simple inflationary models predict a power-law spectrum for the tensor perturbations as well. The ratio of the scalar and tensor power spectra r is called

scalar-to-tensor ratio and it is an important discriminator between different inflationary models (see section 3.2).

2.3.2 Brief History of the Universe

Inflation can produce a nearly scale-invariant primordial fluctuation spectrum with Gaussian statistics. As discussed above, this eventually sets the initial conditions for the structure formation. After inflation ends the inflaton field decays and the energy stored in the inflaton field goes into reheating the universe as the decay products thermalize. At this time the inflaton field fluctuations turn into fluctuations in the various species in the plasma. The spectrum of the large-scale primordial fluctuations is not modified by microphysical processes in the plasma at this time. These are encoded in the curvature perturbations, which is conserved outside the horizon. As universe cooled due to its expansion it underwent several important phases, such as the electroweak phase transition at around 100 GeV temperature and hadronization of the quark-gluon plasma, at around 1 GeV temperature. Then, at around 1 MeV temperature neutrinos decoupled from the plasma forming cosmic neutrino background radiation, and at around same temperature electrons and positrons annihilated. At this point the elementary-particle content of the universe was finally stabilized.

At around 1 MeV temperatures universe was cooled enough for ignition of nuclear fusion in the plasma. This process is called big-bang nucleosynthesis (BBN). During BBN the primordial light-element abundancies are produced. Protons and neutrons in the plasma combined to produce mainly helium, deuterium and lithium. The only cosmological parameter relevant for this process is the baryon-to-photon ratio, otherwise it is the standard low energy nuclear physics that determines the details of the BBN.

Requiring that the predicted hydrogen and helium abundancies satisfy the observational limits determines the baryon-to-photon ratio in a CDM universe at the epoch of nucleosynthesis. While the standard model accommodates neatly the deuterium- and helium abundancies, there is a yet some discrepancy between the observations and the standard model prediction for the lithium abundance. The primordial lithium abundance is measured from poor-metallicity stars within our own galaxy yielding a value of roughly a third of what is expected in the standard big-bang nucleosynthesis model. One possibility is that the observed abundancies are not primordial, and lithium is somehow depleted in these stars, although such mechanisms are not well known. Another explanation is of course that some 'non-standard model' -physics influenced the lithium abundance dur-

ing the big-bang nucleosynthesis [54]. It is interesting to note, that there's also been a suggestion to solve the lithium problem as a variation in the local lithium abundance due to a local large-scale inhomogeneity [55].

After BBN the universe continues to cool and expand. The baryonic plasma is kept ionized by Thomson scattering between protons and electrons. At recombination, which takes place at around 0.3 eV temperature ($z \approx 1100$), when the number of high-energy photons has fallen sufficiently low, the protons and electrons can bind together to form neutral hydrogen. While this process is extended in time, this time scale is cosmologically negligible. For this reason, observationally the recombination is thought of as a surface. At recombination universe becomes visible and the released radiation is observed as the cosmic microwave background radiation.

2.3.3 Concordance ΛCDM Model

The current standard model of cosmology is an FLRW model sourced by cold dark matter [40], [41] and baryons, radiation comprising the cosmic microwave and neutrino background and of dark energy driving the accelerated expansion [56], [57], [4], [58]. According to the most recent Planck data [1], the standard-model parameters (with 68% CL) are

$$\begin{aligned} \Omega_\Lambda &= 0.67^{+0.027}_{-0.023}, \\ \Omega_b h^2 &= 0.02217 \pm 0.00033, \\ \Omega_k &= -0.0096^{+0.010}_{-0.0082}, \\ H_0 &= (67.9 \pm 1.5)\ \ \mathrm{km}\, s^{-1}\, \mathrm{Mpc}^{-1}, \\ n_s &= 0.9635 \pm 0.0094, \\ \theta_* &= (1.19355 \pm 0.00078)^\circ, \end{aligned} \tag{2.40}$$

where θ_* is the current angular scale of the acoustic horizon at the time of recombination.

The primordial fluctuation spectrum generated by inflation sets the initial conditions for density fluctuations in the primordial plasma. This, in turn, is depicted as a linearly perturbed FLRW model, the details of which are determined by the microphysics.

It is well established observationally that universe contains significant amounts of some yet unknown form of dark matter, which does not interact electromagnetically. Observations over very wide range of mass scales, from galactic rotation

curves to velocities of galaxies in clusters and the gravitational lensing due to clusters, imply that these structures should be roughly five times more massive than what can be accounted for by the luminous matter within them [59]. Furthermore, dark matter plays significant role in explaining the structure formation. Before recombination the pressure gradients evened out density fluctuations in the baryon-photon plasma to the point that the smooth distribution of the baryonic density seen in the CMB could not have evolved into dense galactic structures seen today fast enough without some enhancement mechanism. The cold dark matter decoupled from the primordial plasma relatively early, and by the time of recombination the CDM-density fluctuations had evolved into strong gravitational potentials into which the baryonic matter fell after recombination giving the needed enhancement for the structure formation.

The standard model describes the cosmic evolution of the universe quantitatively well after the recombination. The increasing number of type Ia supernovae observations revealed a puzzling fact that on larger redshifts the supernovae appeared to be fainter than expected. In the context of the FLRW model this observation shows that the expansion of the universe is accelerating, constituting the dark-energy problem. With the current parameters, the cosmic evolution has recently transmitted from a matter dominated phase into a phase of accelerating expansion driven by cosmological constant. Extrapolating the model further in time then suggests that the universe is again entering into an exponentially expanding de Sitter -phase.

2.4 Dark Energy

Dark energy can be observationally probed on cosmological scales only. The observation most sensitive to its existence is the magnitude-redshift relation of type Ia supernovae. It appears that (see Fig. 5) the universe has turned into a phase of accelerating expansion roughly at redshift $z \approx 1$. In ΛCDM the value of cosmological constant needs to be fine tuned in order to have universe enter the accelerating expansion that late. This is known as the coincidence problem [60]. It is then quite interesting that at large scales the structure formation has entered non-linear regime also at around $z \approx 1$. Also, the Buchert equations (2.34) and (2.35) show that an inhomogeneous dust cosmology could produce a backreaction term which would lead to apparent acceleration. This tempts us to consider alternatives for dark energy by elaborating the modelling of large-scale structure.

Another fine-tuning problem in the context of ΛCDM concerns the smallness of

the cosmological constant. General relativity contains two fundamental constants of nature $\kappa \equiv 8\pi G$ and Λ, with G being the Newton's gravitational constant and Λ the cosmological constant. The product of these two constants is a dimesionless quantity and in the standard model we have $\kappa\Lambda \approx 4\times 10^{-120}$. Attemps to explain this low value as a vacuum-energy density is problematic since quantum field theory estimates for $\kappa\Lambda_{\text{vacuum}}$ are of order one [60].

There are three generic alternatives to explain the observed apparent acceleration of the universe. The first is some unknown matter component with high enough negative pressure. Second is some modification to general relativity at large distances. Cosmological constant can be interpreted as belonging to either of these two, depending on which side of the Einstein equation the term is interpreted as belonging to. Third possibility is that Λ is an illusion caused by the nonlinear effects due to the cosmic structure, i.e. the backreaction as suggested by the Buchert equations.

2.4.1 Void Models

It has been suggested that,instead of accelerated expansion, the supernovae magnitude-redshift relation could be explained by faster than average expansion locally. In terms of dust-model cosmology, this means that we would live near the center of a deep Gpc scale underdensity [14, 15, 16, 17, 18, 19, 20, 21, 22]. This scenario is easily modelled by use of spherical symmetry. A spherically symmetric inhomogeneous and irrotational dust model, or the Lemaître-Tolman-Bondi model (LTB model) is described by the LTB-metric:

$$\mathrm{d}s^2 = -\mathrm{d}t^2 + \frac{Y'}{1+2E} + Y^2\left(\mathrm{d}\theta^2 + \sin^2\theta \mathrm{d}\phi^2\right). \tag{2.41}$$

Here the angular scale function Y depends on r and t, and the energy function E depends on r only, and prime denotes a partial derivative with respect to r. This form for the metric allows an analytic solution to the Einstein equation (2.8) with a spherically symmetric comoving dust source. The energy-momentum tensor for such a source is

$$T^{\mu\nu} = \rho u^\mu u^\nu, \tag{2.42}$$

where $\rho = \rho(t, r)$ is the dust energy density and $u^\mu = (-1, 0, 0, 0)$ is the dust 4-velocity.

It is in fact easy to build an LTB model which reproduces the observed supernova magnitude-redshift relation. However, simultaneously requiring the model

to satisfy other observational constraints turns out to be difficult. These difficulties are examined in more detail in section 5. Moreover, the density contrast $\delta_M \equiv (\rho_{\text{in}} - \rho_{\text{out}})/\rho_{\text{out}}$, where $\delta_M \equiv (\rho_{\text{in}} - \rho_{\text{out}})/\rho_{\text{out}}$ denotes the dust energy-density contrast between the underdensity center ρ_{in} and the background ρ_{out}, of the Gpc scale underdensity required would have to be of order $\delta_M \propto 10^{-3}$ at recombination. This is roughly two orders of magnitude greater than the fluctuation scale inferred by the CMB temperature anisotropies which implies that such structure would not be of inflationary origin. Also, the fact that we would have to be located very near to the center of the underdensity in order to preserve the observed isotropy of the universe constitutes a new fine-tuning proplem.

Despite these difficulties, the conceptual simplicity of this scenario makes it an interesting alternative for dark energy. However large the underdensity would have to be, it turns out that the present state of observations can not conclusively exclude the *local-void scenario*. It should also be remembered that dark energy itself is very problematic: though the cosmological constant fits with the observations well, its fundamental nature and size remains a complete mystery with a fine-tuning problem of its own. Inflation on the other hand, although seemingly succesful, is a paradigm and ideas about underlying physics remain highly speculative. Moreover, even within the inflationary paradigm such vast structure could in principle find some other than inflationary origin.

3 Cosmic Observables

3.1 Local Expansion Rate

The local expansion rate of the universe is measured from the slope of the velocities of galaxies in our cosmic neighbourhood as a function of distance:

$$v = H_0 r, \tag{3.1}$$

where H_0 is the Hubble constant. In order to observe the linear trend, the galaxies need to be sufficiently far so that they are not gravitationally bound to the local neighbourhood of the observer, and on the other hand not too far so that the linear approximation holds. In practice H_0 is determined from systematic cosmological redshifts of nearby galaxies within a distance of roughly 200 Mpc's [61], [62], [63].

One of the most important distance measurements use the cepheid variables

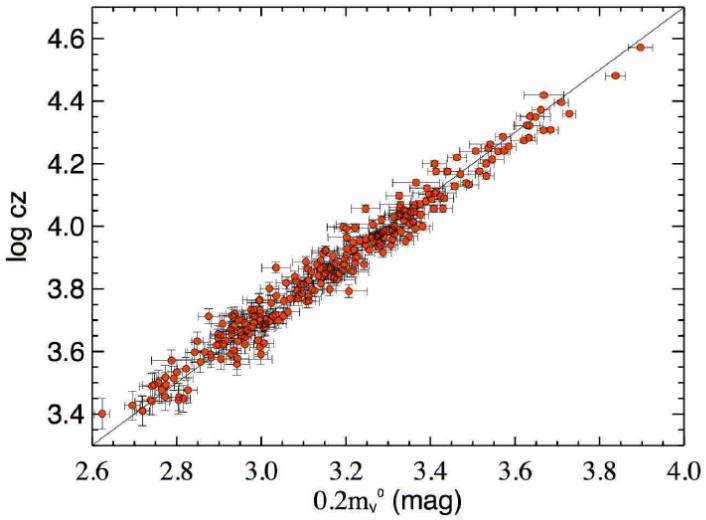

Figure 1: Figure shows the magnitude-redshift data for nearby ($z < 0.1$) type Ia supernovae and the best linear fit yielding the present day determination for the Hubble constant. Figure is taken from Ref. [63].

stars. Cepheids are very bright pulsating stars with a strong correlation between the luminosity and the pulsation period. This makes them good standard candles, which allow extending the cosmic ladder beyond our own galaxy after their luminosities are calibrated with parallax measurements within our local galactic neighbourhood. Cepheids can in turn be used to calibrate the distances to more distant galaxies where another type of much more luminous standard candles are observed, the type Ia supernovae. Figure 1 from Ref. [63] shows a linear fit to the logarithm of the redshift of 240 nearby ($z < 0.1$) type Ia supernovae as a function of their apparent magnitude.

There are also other independent means of measuring the Hubble constant and they support the calibration and results obtained with the cepheid variables and supernovae [65]. One of those uses the stars at the tip of the red giant branch. Others include maser galaxies in which sparse, heating water vapor in the galactic disk acts as a maser source, or Tully-Fisher relation which is based on a correlation between a spiral galaxy's total luminosity and its maximum rotational velocity. Yet there is a surface brightness fluctuation method which is also based on the red giant branch stars but on the statistics of the entire population. All these methods can be used as checks on the determination of the distance scale as well as alternative means of calibration.

The most accurate present-day determination of $H_{\rm loc}$ is given in Ref. [63], based on type Ia supernovae magnitude-redshift relation. Reference [63] gives two determinations for the local Hubble rate. The more accurate one is based on cepheid distance calibration by the maser galaxy NGC 4258 which contains cepheids of wide variety of different metallicities, which affect the absolute magnitude of cepheids. The other one is based on cepheid distance calibration by cepheids found in the Large Magellanic Cloud (LMC). The distance to the LMC can be measured e.g. by the tip of the red giant branch method. However, there is uncertainty in the determination of the distance to the LMC and the cepheids found there are of different metallicities than the ones used for calibration of the supernovae. The value using the LMC calibration is

$$H_{\rm loc} = 73.3 \pm 4.6 \text{km s}^{-1} \text{ Mpc}^{-1}, \tag{3.2}$$

while the more accurate one using the maser-galaxy calibration is

$$H_{\rm loc} = 74.2 \pm 3.6 \text{km s}^{-1} \text{ Mpc}^{-1}. \tag{3.3}$$

Both values are clearly consistent with each other. However, in Ref. [64] the analysis of [63] was critically discussed and they also presented an improved analysis.

3.2 Cosmic Microwave Background

Cosmic microwave background radiation (CMB) is nearly isotropic, almost perfect black-body radiation of roughly 2.725 K temperature observed in all directions in the sky. CMB radiation was formed when the photons were released when initially free, charged protons and electrons recombined into neutral hydrogen atoms. Recombination occured relatively quickly and it turns out that the photons last scattered at around $z \approx 1100$. So the observed photons carry information about the structure of the universe.

Indeed, the temperature fluctuations in the CMB are directly related to the fluctions in the baryonic density on the last-scattering surface. The most accurate map of the CMB up to date has been measured lately by the Planck satellite [1]. Figure 2 shows the CMB temperature map as seen by the Planck satellite after filtering out the foreground noise. Regions shown in blue are colder and those shown in red hotter than the average temperature. The scale of the fluctuations is μK, i.e. $\frac{\Delta T}{T} \propto 10^{-5}$.

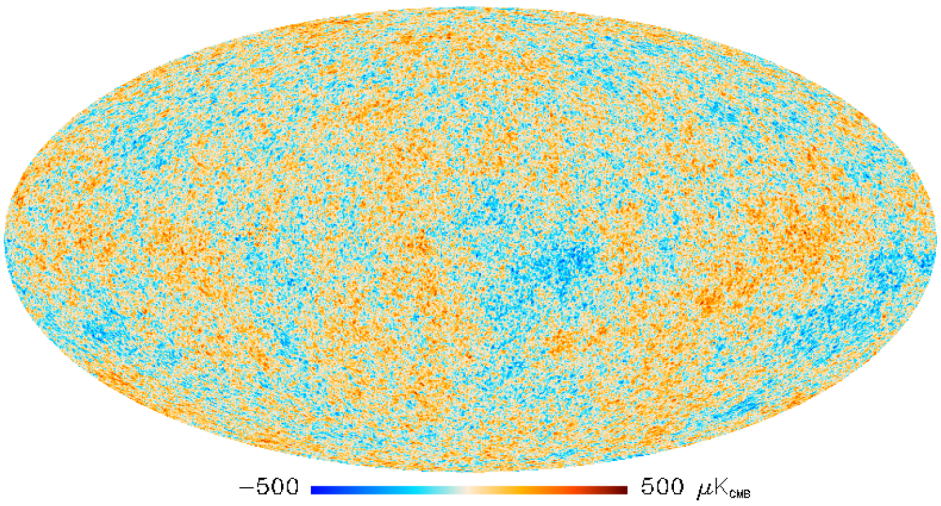

Figure 2: Figure shows the foreground filtered CMB temperature anisotropy map as measured by the Planck satellite. Large areas with hotter or colder temperatures than on average are clearly visible on the map, these are the hot and cold spots. Figure is taken from Ref. [1].

The two dimensional temperature map over the sky is naturally presented in spherical harmonics. Figure 3 shows the acoustic features in the spectrum of such a multipole expansion of the anisotropy map. The location of the first peak in particular is determined by the acoustic horizon in the plasma at the recombination and by the angular-diameter distance to the recombination surface. The observed temperature spectrum is in an excellent agreement with a six parameter ΛCDM model and with the BBN determination of the baryon density [1]. Also, within the context of Friedmannian cosmology, Planck results constrain the spatial curvature to flat within percent level [1].

The Hubble rate can be determined from the CMB data independent of the local measurements. The Planck mission best-fit Hubble rate is $H_0 = (67 \pm 1.2)$ $\mathrm{km\,s^{-1}\,Mpc^{-1}}$ [1] which is significantly lower than the local determination of Eq. 3.3. The origin of this discrepancy remains unclear. This creates some tension in the ΛCDM model but it would be naturally explained by a shallow, local large-scale underdensity in the matter distribution.

Inflationary models predict also a power-law spectrum of gravitational waves, i.e. tensor perturbations. The ratio of the amplitudes of the tensor and scalar power spectra at some scale is called scalar-to-tensor ratio r. This ratio can be measured from the Planck CMB temperature anisotropy map and from the

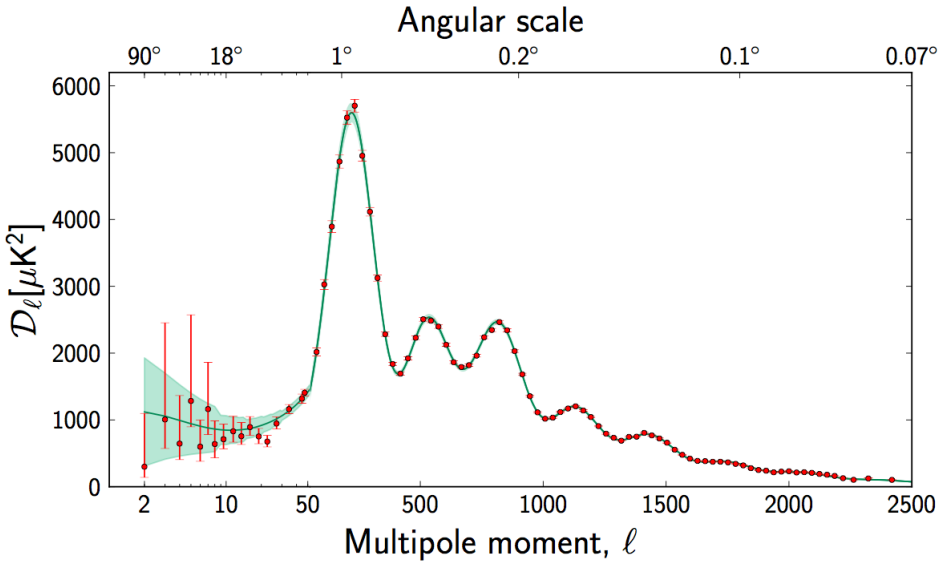

Figure 3: CMB multipole expansion spectrum. Figure is taken from Ref. [1].

CMB polarization data. Figure 4 shows constraints on the (n_s, r)-plane drawn from the temperature-anisotropy data alone together with plausible parameter areas for simple inflationary models. However, BICEP 2 [67] favors roughly a scalar-to-tensor ratio of 0.2 and is at 1.3σ discrepancy with the Planck result [68].

3.3 Type Ia Supernovae

Let us return to discuss the use of type Ia supernovae as standard candles. The progenitors of these objects are white dwarfs in binary star systems, which are brought over the critical mass by accretion of gas from the companion star. Because of their similar birth mechanism their intrinsic luminosites should also be similar, which is what makes them potentially good standard candles.

The most thorough supernovae cataloque to date is the Union2.1 SNe compilation [69]. However, here we consider the earlier Union 2 compilation [70] which was also used in papers [I] and [III]. It consists of data from 557 type Ia supernovae in the redshift range $z = 0.015 - 1.4$. Because the cepheid variable population starts getting sparse at redshifts at which the type Ia supernovae start getting abundant there are only a few cepheids to calibrate the supernovae distances. In fact the

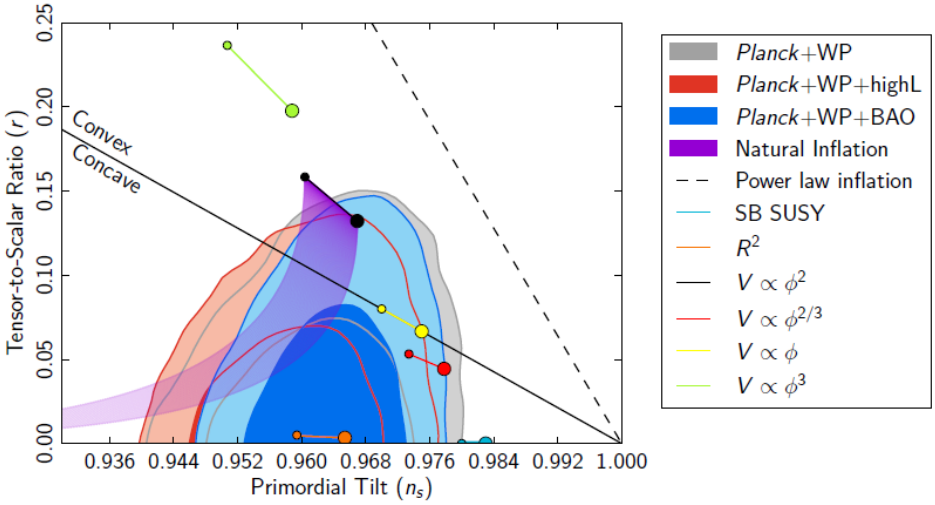

Figure 4: Figure shows the marginalized likelihood with 95% and 68% confidence levels on (n_s,r)-plane. Figure is taken from Ref. [1].

magnitudes of the supernovae are calibrated by only six cepheid variables each of which shares the host galaxy with a type Ia supernova [65]. Figure 5 shows the data points of the Union2 compilation with the distance-modulus-redshift relation of the best fit ΛCDM-model.

It is interesting to note that the type Ia supernovae data shows hemispherical asymmetries in the Hubble diagram of $\Delta H_0/H_0 \approx 10\%$, with statistical significance at the 95% C.L. [60]. It is yet unclear, if it is not just simply a statistical fluctuation, whether this sould be regarded as an indication of violation of isotropy in the local neighbourhood or if it is just due to some unknown systematic issue in the observations.

3.4 Observable signals from inhomogeneities

Observables introduced in previous subsections provide model independent signals about local and global features of the universe. However, the intervening inhomogeneous matter content affects the properties of light passing through the structure. This is expected to produce obsevable signals in systematic fashion because the matter distribution displays statistical homogeneity and isotropy. This makes the large-scale structure itself an important cosmological probe.

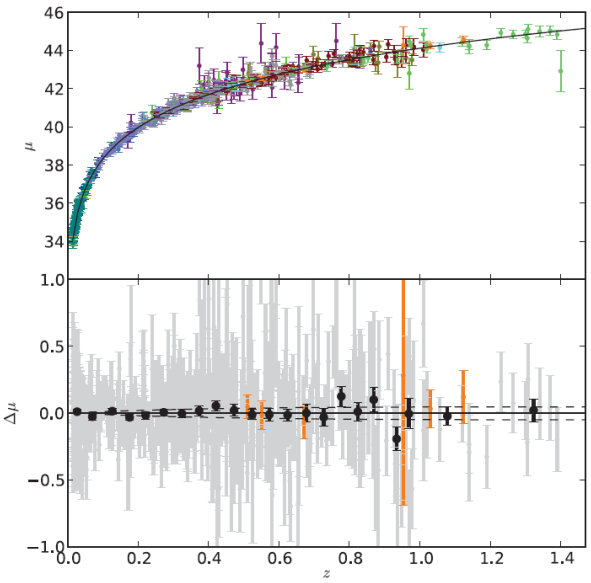

Figure 5: In the upper panel we have the type Ia supernova magnitude-redshift relation from the Union 2 compilation. The curve is for the best-fit ΛCDM model. The lower panel shows residuals from the data points (grey points for individual SNe and black for bins) when the best-fit model is subtracted from the peak magnitudes. Figure is taken from Ref. [70].

3.4.1 kSZ effect

CMB photons scatter off free electrons in the intergalactic medium. The systematic effect on the CMB map due to this phenomenom is called the kinematic Sunyaev-Zeldovich effect (kSZ effect). The magnitude of the effect depends on the peculiar velocities of galaxies with respect to the CMB restframe. While in an FLRW model the CMB remains isotropic everywhere, thus making the kSZ effect a perturbative quantity, in inhomogeneous models the general isotropy is lost. Large-scale inhomogeneities induce large peculiar velocities and the local CMB dipole responsible for the kSZ effect can be decomposed into contributions due to the inhomogeneous background and perturbative velocities [24]. So the kSZ effect can be used to detect and constrain the large-scale structure. On the other hand, the Copernican principle itself can be revoked and constrained by kSZ observations by detecting or constraining peculiar velocities accociated with local bulk flow of the matter density. In this context the kSZ effect has been studied in Ref's. [23], [24], [71], [25].

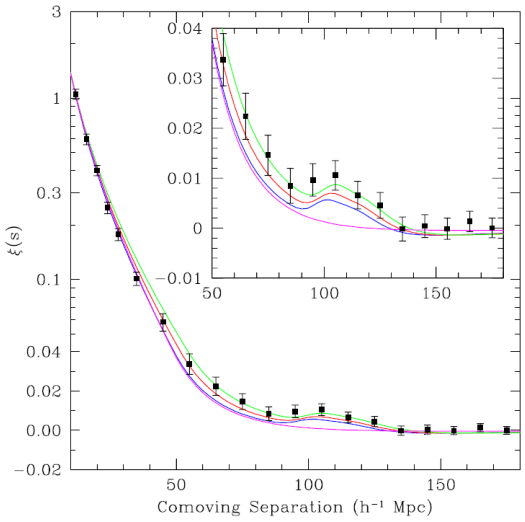

Figure 6: Figure shows linearly perturbed FLRW model predictions for the two-point correlation function as a function of the comoving separation on the redshift $z = 0.35$ slice and results for the correlation function drawn from the same redshift slice of the SDSS-data. The shown models from top down are $\Omega_M h^2 = 0.12$ (green), 0.13 (red), and 0.14 (blue), all with $\Omega_b h^2 = 0.024$ and $n_s = 0.98$. The bottom line (magenta) lacking the bump is a pure CDM model with $\Omega_M h^2 = 0.105$. Figure is taken from Ref. [75].

3.4.2 SW and ISW -effects

Gravitational potentials directly influence photon properties. The Sachs-Wolfe effect (SW effect) refers to the linear contribution to the gravitational redshift of photons due to the gravitational potential of the source. The integrated Sachs-Wolfe effect (ISW effect) refers to the total gravitational redshift due to all potentials between the source and observer. For a continuous, spherically symmetric dust inhomogeneity the ISW effect vanishes for an observer outside the inhomogeneity looking through it, unless there is some form of dark energy to unbalance the compensating effects of the profile. Therefore, the ISW effect is considered a prominent observable to have another independent, direct detection of the dark energy.

3.4.3 Stacked ISW-effect

A signal from the ISW-effect can be extracted by comparing the CMB-map at the positions and solid angles subtended by large-scale structures identified from galaxy catalogues. Such signal is called stacked ISW-effect.

The Planck collaboration [1] reported roughly a 3σ detection of a stacked ISW-signal, under the flat Friedmannian prior, compatible with signal detected from the WMAP data [73]. Under the same prior, the Planck collaboration reports also an ISW detection of $\approx 2.5\sigma$ from CMB alone by cross-correlating secondary anisotropies with the lensing signal [1]. Along with the Planck results, the detection of an ISW signal provides strong complementary evidence for accelerating late time expansion, and thus for $\Omega_\Lambda \approx 0.7$ under the flat ΛCDM prior.

3.4.4 BAO scale

Baryon acoustic oscillations (BAO) are the imprint of acoustic oscillations in the primordial baryonic plasma on the three dimensional spatial distribution of galaxies [74], [75], [76]. BAO feature was generated before recombination in the baryon-photon plasma by the same mechanism that created the acoustic feature in the CMB-spectrum. This imprint can be observed from the galaxy distribution as seen today. Indeed, the SDSS luminious-red-galaxy sample shows the acoustic baryonic feature on the galaxy distribution in the two-point-correlation function. Figure 6 shows the data for the two-point correlation function on a redshift $z = 0.35$ slice of the SDSS galaxy catalogue, fitted with predictions from different linearly perturbed FLRW models. The FLRW models shown in the figure are flat ΛCDM models. Parameters Ω_M, Ω_b are present-day density parameters for total-dust-, and baryon densities, respectively. The dimensionless Hubble parameter h is just the local Hubble rate in units of 100 (km/s)/Mpc. The data clearly shows a bump at 115 Mpc's on the comoving scale. This feature is reproduced by FLRW models with sufficient baryonic matter content. However, the model independent significance of this detection has been under dispute [77].

3.5 Large-scale structure

On large scales the matter density of the universe has evolved into dense filamentary structures encircling large and empty voids. Understanding the formation of this weblike structure is crucial to cosmology. Not only because of its role in

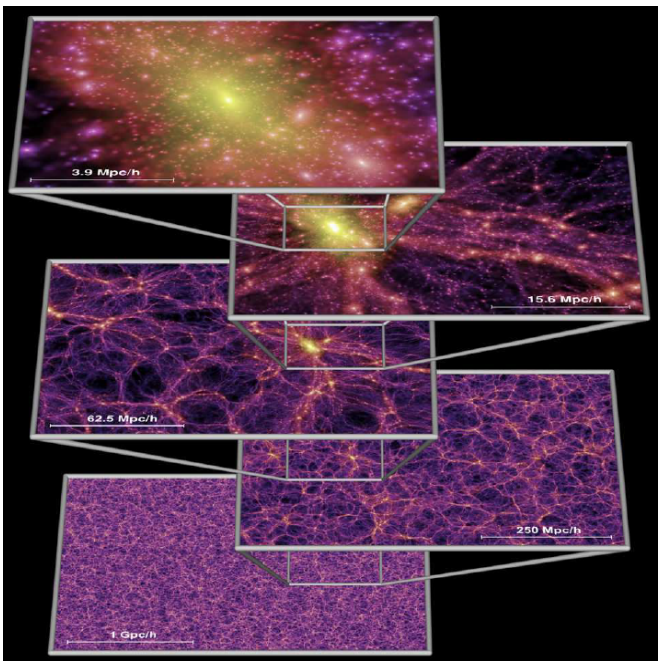

Figure 7: Figure shows the detailed large-scale structure of the universe on various length scales as seen in N-body simulations. Figure is taken from Ref. [5].

giving birth to signals described in previous subsection, but also because it is an observable probe for the cosmological model in itself. There are several ways to obtain explicit information about the matter distribution on large scales.

3.5.1 N-body Simulations

Large-scale N-body simulations [5] (see Fig. 7) have shown that nearly Gaussian initial conditions for the matter distribution and scale invariant power spectrum evolve into a web-like structure with thick filaments and sheets surrounding empty, expanding voids. This is also exactly what is seen in the galaxy catalogues examples of which are shown in Fig. 8. Dark matter forms the backbone of this *cosmic web*, towards which the baryonic matter is drawn under the influence of gravity.

3.5.2 Lyman-α -forest

Large-scale structure can also be probed by the absorption line structure in the spectrum of light emitted by distant quasars. Indeed the diffuse baryonic gas component present on large-scale structure induces Lyman-α absorption lines at different wavelengths at different redshifts to the spectrum of light passing through filamentary structures. The detailed form of this so-called Lyman-α forest provides important complementary information about the large-scale structure at high redshifts in addition to galaxy cataloques, lensing studies and N-body simulations.

3.5.3 Weak Lensing

Yet more information about the local large-scale structure can be obtained from the distortions of the images of galaxies due to the weak lensing by the gravitational field of the cosmic web [78]. The statistics of weak lensing provides high precision measurement given a large enough sample. As the distortions depend essentially only on the gravitational field in the intergalactic space, the signal is also largely independent of galactic astrophysics [78]. The latest SDSS cataloque [2] comprises data from almost a million of galaxies. The distortions in the images of distant galaxies shows systematic alignment depending on the intervening matter content. For this reason the weak lensing produces a signal probing the matter distribution.

3.5.4 Superstructures

Large quasar groups are the largest structures observed in the universe, extending over hundreds of megaparsecs. These structures, seen in relatively early universe, are probably seeds for superclusters and supercluster complexes, such as the Sloan Great Wall observed at $z \approx 0.073$ (see Fig. 8). There exists even putative observations of extremely large quasar groups (LGQ's), extending up to Gigaparsec scales [26], [27]. The largest of these has a characteristic size of 500 Mpc's, extends well over one Gpc in the longest dimension, and is estimated to have density contrast roughly between 1.2 and 1.4 [27]. The characteristic size is just the cubic root of the proper volume today (under the ΛCDM prior). On the other hand, homogeneity scale in ΛCDM, backed up by the SDSS data [28], is reached at around 60 Mpc's. This suggests that the local spacetime metric associated with structures of this size deviates significantly from the global ΛCDM

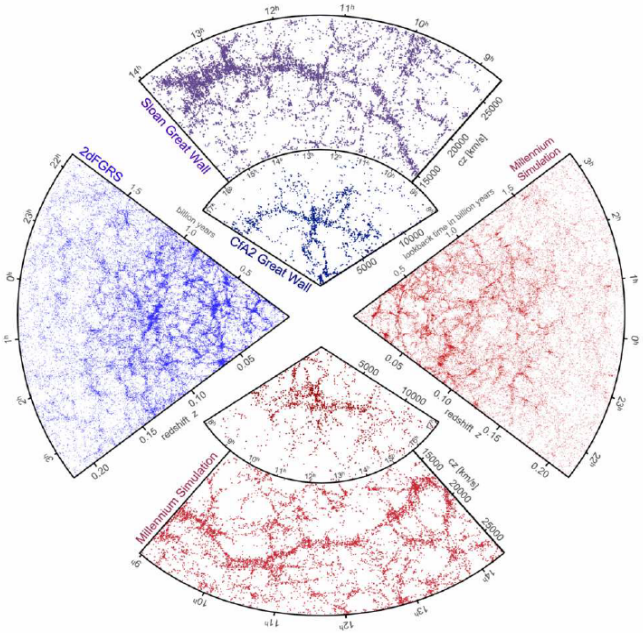

Figure 8: Figure shows slices of galaxy cataloques, illustrating the local structure of the universe, drawn from 2df and SDSS surveys, and from the millenium simulation. The Sloan great wall is the dense structure shown in the uppermost slice. Figure is taken from Ref. [78].

metric also on cosmological scales.

Other superstructures have been observed in the CMB. Exeptionally large cold and hot spots seen in the CMB temperature map indeed seem to imply existence of very large structures. The foreground-corrected CMB data shows low-multipole anomalies including large cold spots extending up to ten degrees in angular diameter. These anomalies have been suggested to be (for the cold spots) due to large and empty voids with sizes up to $300h^{-1}$ Mpc's between the last-scattering surface and the observer [29, 30, 31, 32]. In this case the "coldness of the spot" would result due to the integrated Sachs-Wolfe effect.

However, the structures causing the CMB-anomalies do not neccessarily have to lie between us and the last-scattering surface, but they could also reside on the last-scattering surface itself. Indeed, the amplitudes of the hot and cold spots are of order 10^{-5}, i.e. they are perfectly compatible with the almost flat power spectrum. If these spots were to be originated due to structures on the recombination surface, in which case they would result due to the Sachs-Wolfe effect, the cold spots would correspond to overdensities (and hot spots to underdensities).

The sizes of the corresponding structures in the latter case were estimated e.g. in [30], with a conclusion that in this case the corresponding inhomogeneities are again of Gpc scale in diameter.

In conclusion, the statistical homogeneity in our cosmic neighbourhood is not yet established up to Gpc scales. This rises a question about the intepretation of cosmological data: If the local homogeneity is violated on Gpc scales, how much the FLRW prior misleads us in estimating the cosmological parameters? The first approximate answers to this issue can be obtained by studies invoking spherical symmetry.

4 Spherically Symmetric Perfect Fluids

In this section the dynamics of spherically symmetric multi-component perfect fluids are studied using the ADM formalism. The model is the same as in Ref. [II], but system of equations derived here is free from numeric problems encountered in [II]. Thus, the system of equations derived is readily solvable for wider range of models. Subsection 4.4 contains an unpublished result on how to set initial conditions for initially super Hubble inhomogeneities in a general multi-component models. Previous approaches in the literature have only made use of the exactly solvable condition for the LTB model.

4.1 Metric and Source

The most general spherically symmetric metric written in the ADM form (2.11) is

$$\mathrm{d}s^2 = -\alpha^2 \mathrm{d}t^2 + h_{rr}\left(\beta^r \mathrm{d}t + \mathrm{d}r\right)^2 + h_{\theta\theta}\mathrm{d}\Omega^2. \tag{4.1}$$

Here α is the lapse function, β^r is the radial shift function. These, as well as the angular and radial metric components $h_{\theta\theta}$ and h_{rr} are functions of coordinates t and r. In order to keep the equations simple we choose to work in a shiftless gauge, where $\beta^r = 0$. In this gauge the metric (4.2) becomes exactly of the same form as the Lemaître metric [79, 80, 81]:

$$\mathrm{d}s^2 = -e^{2\lambda}\mathrm{d}t^2 + \frac{Y'^2}{1+2E}\mathrm{d}r^2 + Y^2\mathrm{d}\Omega^2, \tag{4.2}$$

where we made the replacements: $\alpha \equiv e^{\lambda}$, $h_{\theta\theta} \equiv Y^2$ and $h_{rr} = \frac{Y'^2}{1+2E}$. These

variables were used in paper [II]. Here we will start directly with the ADM formulation, because it leads to a system which is numerically more easily solvable.

The energy-momentum tensor for a perfect fluid in the coordinate basis reads

$$T^{\mu\nu} = (\rho + p)u^\mu u^\nu + pg^{\mu\nu}, \tag{4.3}$$

where u^μ is the fluid four velocity, normalized as $u^2 = -1$, and ρ and p are the fluid energy and pressure densities, respectively. For a spherically symmetric fluid

$$u^\mu = \gamma\left(\frac{1}{\alpha}, v_c, 0, 0\right) = \gamma\left(\frac{1}{\alpha}, \frac{v_p}{\sqrt{h_{rr}}}, 0, 0\right), \tag{4.4}$$

where v_c is the radial comoving velocity field of the fluid, and $v_p = \sqrt{h_{rr}}v_c$ is the corresponding proper velocity, and $\gamma \equiv 1/\sqrt{1 - v_p^2}$ is the corresponding Lorentz boost factor. Functions ρ, p and v_c are also to be understood as functions of coordinates t and r. Metric of Eq. (4.2) can be sourced by a tensor sum of spherically symmetric perfect-fluid components. In principle there could be couplings between different components, but here we will assume that all components satisfy energy-momentum tensor conservation equation individually. Constraining the source to a comoving dust, i.e. $v_c = 0$ and $p = 0$ imposes $\alpha \equiv 1$, and by the Einstein equation (2.8)

$$h_{rr} = C(r)\frac{h_{\theta\theta,r}^2}{4h_{\theta\theta}}, \tag{4.5}$$

yielding the LTB metric 2.41. If the source fluids are also homogeneous we further find:

$$h_{rr} = \frac{a(t)^2}{1 - kr^2} \tag{4.6}$$

$$h_{\theta\theta} = a(t)^2 r^2, \tag{4.7}$$

yielding the FLRW metric (2.23). The condition $\alpha \equiv 1$ for the lapse function is called a geodetic slicing. It specifies a freely falling coordinate system up to a radial comoving velocity v_c between the source and the coordinate system.

The independent, non-vanishing components of the energy-momentum tensor for n perfect-fluid components such as in Eq. (4.3), with four-velocities as in Eq.

(4.4), in the spherically symmetric case are

$$\begin{aligned} T_{tt} &= \sum_{i=1}^{n} \alpha^2 \gamma_i^2 (\rho_i + v_{i,p}^2 p_i), \\ T_{tr} &= -\sum_{i=1}^{n} \alpha \sqrt{h_{rr}} \gamma_i^2 v_{i,p} (\rho_i + p_i), \\ T_{rr} &= \sum_{i=1}^{n} \left(h_{rr} \gamma_i^2 v_{i,p}^2 (\rho_i + p_i) + h_{rr} p_i \right), \\ T_{\theta\theta} &= \sum_{i=1}^{n} h_{\theta\theta} p_i. \end{aligned} \tag{4.8}$$

It is useful to define an effective gravitational mass $F = F(t, r)$ in a spherically symmetric model as the mass parameter of the Schwarzschild metric, which at a given time t and radius r smoothly joins the corresponding interior metric (4.2). For the metric (4.2), the effective gravitational mass is given by [83, 84, 82]

$$F = \pi \alpha^2 \frac{\dot{h}_{\theta\theta}^2}{h_{\theta\theta}^{3/2}} - \pi \frac{h_{\theta\theta,r}^2}{h_{rr} \sqrt{h_{\theta\theta}}} + 4\pi \sqrt{h_{\theta\theta}}. \tag{4.9}$$

Next we write down the ADM equations given in section 2.1.5 for the variables h_{rr}, $h_{\theta\theta}$, K_{rr} and $K_{\theta\theta}$. The independent source terms appearing in the ADM equations, following from the projections of Eq. (2.20) for a radially symmetric n fluid-component energy-momentum tensor as in Eq. (4.8) are given by:

$$\begin{aligned} \rho &= \frac{1}{\alpha^2} T^{tt}, \\ S_r &= \frac{1}{\alpha} T_{tr}, \\ M_{rr} &= \frac{1}{2} \frac{h_{rr}}{\alpha^2} T_{tt} + \frac{1}{2} T_{rr} - \frac{h_{rr}}{h_{\theta\theta}} T_{\theta\theta}, \\ M_{\theta\theta} &= \frac{1}{2} \frac{h_{\theta\theta}}{\alpha^2} T_{tt} - \frac{1}{2} \frac{h_{\theta\theta}}{h_{rr}} T_{rr}. \end{aligned} \tag{4.10}$$

The equations of motion (2.16) here become the following four independent equa-

tions for metric components h_{rr}, $h_{\theta\theta}$ and extrinsic curvatures K_{rr} and $K_{\theta\theta}$:

$$\begin{aligned}
\dot{h}_{rr} &= -2\alpha K_{rr}, \\
\dot{h}_{\theta\theta} &= -2\alpha K_{\theta\theta}, \\
\dot{K}_{rr} &= -\alpha_{,rr} + \frac{1}{2}\frac{\alpha_{,r}h_{rr,r}}{h_{rr}} + \alpha\Bigg(- \frac{h_{\theta\theta,rr}}{h_{\theta\theta}} + \frac{1}{2}\left(\frac{h_{\theta\theta,r}}{h_{\theta\theta}}\right)^2 + \frac{1}{2}\frac{h_{rr,r}h_{\theta\theta,r}}{h_{rr}h_{\theta\theta}} \\
&\quad - \frac{K_{rr}^2}{h_{rr}} + 2\frac{K_{rr}K_{\theta\theta}}{h_{\theta\theta}} - M_{rr}\Bigg), \\
\dot{K}_{\theta\theta} &= -\frac{1}{2}\frac{\alpha_{,r}h_{\theta\theta,r}}{h_{rr}} + \alpha\Bigg(\frac{1}{4}\frac{h_{rr,r}h_{\theta\theta,r}}{h_{rr}^2} - \frac{1}{2}\frac{h_{\theta\theta,rr}}{h_{rr}} + \frac{K_{rr}K_{\theta\theta}}{h_{rr}} \\
&\quad + 2\left(\frac{K_{\theta\theta}}{h_{\theta\theta}}\right)^2 + 1 - M_{\theta\theta}\Bigg).
\end{aligned} \tag{4.11}$$

The constraint equations (2.21) and (2.22) on the other hand give rise to the *Hamiltonian constraint*:

$$2\rho + 2\frac{h_{\theta\theta,rr}}{h_{rr}h_{\theta\theta}} - \frac{1}{2}\frac{h_{\theta\theta,r}^2}{h_{rr}h_{\theta\theta}^2} - \frac{h_{rr,r}h_{\theta\theta,r}}{h_{rr}^2h_{\theta\theta}} - 4\frac{K_{rr}K_{\theta\theta}}{h_{rr}h_{\theta\theta}} - 2\left(\frac{K_{\theta\theta}}{h_{\theta\theta}}\right)^2 - \frac{2}{h_{\theta\theta}} = 0, \tag{4.12}$$

and the *momentum constraint*

$$S_r - 2\frac{K_{\theta\theta,r}}{h_{\theta\theta}} + \frac{h_{\theta\theta,r}}{h_{\theta\theta}}\left(\frac{K_{rr}}{h_{rr}} + \frac{K_{\theta\theta}}{h_{\theta\theta}}\right) = 0. \tag{4.13}$$

First, it turns out that $h_{\theta\theta}$ behaves as r^2 near the origin, as expected from the homogeneous limit. We then notice that the two first terms in parenthesis on the right-hand side of the $\dot{K}_{\theta\theta}$-equation in (4.11) both diverge at the origin. The terms cancel each other exactly, but such cancellation is difficult to achieve to high accuracy numerically. In order to cast the equations to a numerically more manageable form we need to handle such cancellations analytically. To do this we make the change of variable:

$$h_{\theta\theta} \to H_{\theta\theta}^2. \tag{4.14}$$

The variable $H_{\theta\theta}$ then is actually exactly the same as the scale factor Y of paper II. The two problematic terms then become

$$-\frac{h_{\theta\theta,rr}}{h_{\theta\theta}} + \frac{1}{2}\left(\frac{h_{\theta\theta,r}}{h_{\theta\theta}}\right)^2 = -2\frac{H_{\theta\theta,rr}}{H_{\theta\theta}}.$$

This combines the two cancelling terms into one and of course, as $h_{\theta\theta} \propto r^2$, $H_{\theta\theta} \propto r$ and thus the term on the right-hand side vanishes at the origin. In addition it is convenient to change the variable h_{rr} into its square root, and change the extrinsic curvatures into their mixed-form components i.e.

$$h_{rr} \rightarrow H_{rr}^2 \tag{4.15}$$
$$K_{rr} \rightarrow h_{rr}K^r{}_r \tag{4.16}$$
$$K_{\theta\theta} \rightarrow h_{\theta\theta}K^\theta{}_\theta. \tag{4.17}$$

The mixed components of the extrinsic curvature $K^r{}_r$ and $K^\theta{}_\theta$ are, respectively, just the negative of the longitudinal and transversal Hubble rates defined in paper [II]. With these changes of variables the source terms (4.11) eventually read

$$\begin{aligned}
\rho &= \sum_{i=1}^{n} \gamma_i^2(\rho_i + v_{i,p}^2 p_i), \\
S_r &= -H_{rr} \sum_{i=1}^{n} \gamma_i^2 v_{i,p}(\rho_i + p_i), \\
M_{rr} &= \frac{1}{2}H_{rr}^2 \sum_{i=1}^{n} \left(\rho_i - p_i + 2\gamma_i^2 v_{i,p}^2(\rho_i + p_i)\right), \\
M_{\theta\theta} &= \frac{1}{2}H_{\theta\theta}^2 \sum_{i=1}^{n} (\rho_i - p_i).
\end{aligned} \tag{4.18}$$

Since $H_{\theta\theta} \propto r$ at the origin, it is convenient to make yet another change of variables:

$$H_{\theta\theta} \rightarrow r\hat{H}_{\theta\theta} \tag{4.19}$$

and use a notation

$$X \equiv \frac{H_{\theta\theta,r}}{H_{rr}}. \tag{4.20}$$

With these definitions, and using (4.18) the dynamical equations can be written

as

$$\begin{aligned}
\dot{H}_{rr} &= -\alpha H_{rr} K^r{}_r, \\
\dot{\hat{H}}_{\theta\theta} &= -\alpha \hat{H}_{\theta\theta} K^\theta{}_\theta, \\
\dot{K}^r{}_r &= -\frac{\alpha_{,rr}}{H_{rr}^2} + \frac{\alpha_{,r} H_{rr,r}}{H_{rr}^3} + \alpha\Bigg(- \frac{2}{H_{rr}\hat{H}_{\theta\theta}} \frac{X_{,r}}{r} + (K^r{}_r)^2 + 2K^r{}_r K^\theta{}_\theta \\
&\quad -\frac{1}{2}\sum_{i=1}^{n} \left(\rho_i - p_i + 2\gamma_i^2 v_{i,p}^2 (\rho_i + p_i)\right) \Bigg), \\
\dot{K}^\theta{}_\theta &= -\frac{\alpha_{,r}}{H_{rr}\hat{H}_{\theta\theta}} \frac{X}{r} + \alpha\Bigg(- \frac{1}{H_{rr}\hat{H}_{\theta\theta}} \frac{X_{,r}}{r} + \frac{1}{\hat{H}_{\theta\theta}^2} \frac{1-X^2}{r^2} + K^r{}_r K^\theta{}_\theta \\
&\quad +2\left(K^\theta{}_\theta\right)^2 - \frac{1}{2}\sum_{i=1}^{n} (\rho_i - p_i) \Bigg),
\end{aligned} \tag{4.21}$$

and the constraint equations as

$$\frac{2}{H_{rr}\hat{H}_{\theta\theta}} \frac{X_{,r}}{r} - \frac{1}{\hat{H}_{\theta\theta}^2} \frac{1-X^2}{r^2} - 2K^r{}_r K^\theta{}_\theta - \left(K^\theta{}_\theta\right)^2 = -\sum_{i=1}^{n} \gamma_i^2 (\rho_i + v_{i,p}^2 p_i) \tag{4.22}$$

and

$$2K^\theta{}_{\theta,r} - 2\left(\frac{\hat{H}_{\theta\theta,r}}{\hat{H}_{\theta\theta}} - \frac{1}{r}\right)\left(K^r{}_r + K^\theta{}_\theta\right) = -H_{rr} \sum_{i=1}^{n} \gamma_i^2 v_{i,p} (\rho_i + p_i). \tag{4.23}$$

One can now use Eq. (4.23) to solve for $K^r{}_r$ in terms of $K^\theta{}_\theta$ and $\hat{H}_{\theta\theta}$:

$$K^r{}_r = K^\theta{}_\theta + \frac{r\hat{H}_{\theta\theta}}{r\hat{H}_{\theta\theta,r} + \hat{H}_{\theta\theta}} \left(K^\theta{}_{\theta,r} + \frac{H_{rr}}{2} \sum_{i=1}^{n} \gamma_i^2 v_{i,p} (\rho_i + p_i) \right). \tag{4.24}$$

We can thus drop the equation for $\dot{K}^r{}_r$. Dividing the Hamiltonian constraint by two and adding it within the parenthesis on the right-hand side of the equation for $\dot{K}^\theta{}_\theta$ in (4.21) yields

$$\dot{K}^\theta{}_\theta = -\frac{\alpha_{,r}}{H_{rr}\hat{H}_{\theta\theta}} \frac{X}{r} + \alpha \left(\frac{1}{2\hat{H}_{\theta\theta}^2} \frac{1-X^2}{r^2} - \frac{1}{2}\left(K^\theta{}_\theta\right)^2 + \frac{1}{2}\sum_{i=1}^{n} \gamma_i^2 \left(v_{i,p}^2 \rho_i + p_i\right) \right). \tag{4.25}$$

The term proportional to $(1-X^2)/r^2$ is apparently still problematic. It must be finite, but its finiteness only follows from two divergent terms cancelling one another at the origin. In variables $H_{\theta\theta}$, $H_{rr} = \frac{H_{\theta\theta,r}}{\sqrt{1+2E}}$, used in paper [II], we observe that $1-X^2 = -2E$ so that it is useful to make the following change of variables: $H_{rr} \to \frac{H_{\theta\theta,r}}{\sqrt{1+2r^2\tilde{E}}}$. With these manipulations and changes of variables, and using Eq. (4.24) to solve for $K^r{}_r$, the system of equations for variables $\hat{H}_{\theta\theta}$, $K^\theta{}_\theta$ and $\tilde{E}$ finally becomes:

$$\begin{aligned}
\dot{\hat{H}}_{\theta\theta} &= -\alpha \hat{H}_{\theta\theta} K^\theta{}_\theta, \\
\dot{K}^\theta{}_\theta &= -\frac{\alpha_{,r}(1+2r^2\tilde{E})}{r(r\hat{H}_{\theta\theta})_{,r}\hat{H}_{\theta\theta}} + \alpha\left(-\frac{\tilde{E}}{\hat{H}^2_{\theta\theta}} + \frac{3}{2}\left(K^\theta{}_\theta\right)^2 + \frac{1}{2}\sum_{i=1}^{n}\gamma_i^2\left(r^2\tilde{v}_i^2\rho_i + p_i\right)\right), \\
\dot{\tilde{E}} &= \frac{1}{2}\alpha\hat{H}_{\theta\theta}\sqrt{1+2r^2\tilde{E}}\sum_{i=1}^{n}\gamma_i^2\tilde{v}_i\left(\rho_i+p_i\right) - \frac{\alpha_{,r}(1+2r^2\tilde{E})\hat{H}_{\theta\theta}K^\theta{}_\theta}{r(r\hat{H}_{\theta\theta})_{,r}},
\end{aligned} \tag{4.26}$$

where $\tilde{v}_i \equiv \frac{v_{i,p}}{r}$. This is a complete set of equations when the sources are defined. However, we are still left with the Hamiltonian constraint

$$\sum_{i=1}^{n}\gamma_i^2(\rho_i + r^2\tilde{v}_i^2 p_i) + \frac{2}{(r\hat{H}_{\theta\theta})_{,r}\hat{H}_{\theta\theta}}\left(2r\tilde{E} + r^2\tilde{E}_{,r}\right) + \frac{2\tilde{E}}{\hat{H}^2_{\theta\theta}} - 2K^r{}_r K^\theta_\theta - \left(K^\theta{}_\theta\right)^2 = 0, \tag{4.27}$$

which we did not use to reduce the number of variables. It can be, however, used as a check to monitor that the numerical solution remains correct during the time evolution.

Equations (4.26) must be complemented by equations for the source terms. These follow from the conservation of energy-momentum tensor.

4.2 Stress-Energy Conservation

Indeed, as we are considering an ideal fluid source comprised of n decoupled components, where each component is conserved individually:

$$\nabla_\nu T_i^{\mu\nu} = 0, \tag{4.28}$$

where ∇_μ denotes the covariant derivative. From here on we'll drop the i indices, but it is to be understood that following equations hold for each component sep-

arately. The components of these equations (see paper [II]) give rise to the relativistic energy-conservation and Euler equations, respectively, for non-comoving fluids:

$$\frac{d\rho}{d\tau} = -\Theta\,(\rho + p)\,, \tag{4.29}$$

$$\frac{dp}{d\sigma} = -a\,(\rho + p)\,, \tag{4.30}$$

where Θ and a are the expansion and acceleration scalars, respectively, related to expansion tensor and four-acceleration to be defined below. On the left-hand side we have convective derivatives with respect to the proper time τ, and with respect to σ along the four-acceleration a^μ e.g.:

$$\frac{d}{d\tau} \equiv u^\mu \partial_\mu = \frac{\gamma}{\alpha}\frac{\partial}{\partial t} + \frac{\gamma v_p}{H_{rr}}\frac{\partial}{\partial r}\,, \tag{4.31}$$

$$\frac{d}{d\sigma} \equiv \frac{a^\mu}{a}\partial_\mu = \frac{\gamma v_p}{\alpha}\frac{\partial}{\partial t} + \frac{\gamma}{H_{rr}}\frac{\partial}{\partial r}\,. \tag{4.32}$$

Note that in the rest frame of the fluid component the derivative with respect to τ reduces to $\alpha^{-1}\,\partial/\partial t$ and the derivative with respect to σ to $H_{rr}^{-1}\,\partial/\partial r$. We will use this for the dust component. Eq. (4.30) is indeed just a contracted form of the standard Euler equation, which in general reads $h^{\mu\nu}\partial_\nu p = -a^\mu\,(\rho + p)$. From Eq. (4.30) it is clear that the four-velocity of a dust ($p = 0$) component is geodesic.

The nonzero components of the four acceleration of a fluid component, in general defined as $a_\mu \equiv u^\nu\,\nabla_\nu u_\mu$ are given by:

$$a_t = -\alpha\gamma\, v_p\, a \qquad \text{and} \qquad a_r = \gamma\, H_{rr}\, a\,. \tag{4.33}$$

Here the acceleration scalar a is defined as

$$a = \sqrt{g^{\alpha\beta} a_\alpha a_\beta} = v_p^{-1}\Big(\Theta_T + v_p^2\,\Theta_R\Big)\,, \tag{4.34}$$

and Θ_T and Θ_R are again related to expansion tensor $\Theta_{\mu\nu}$ defined as:

$$\Theta_{\mu\nu} = q^\alpha{}_\mu q^\beta{}_\nu\,\nabla_{(\alpha} u_{\beta)} = \nabla_{(\mu} u_{\nu)} + a_{(\mu} u_{\nu)}. \tag{4.35}$$

The quantity $q_{\mu\nu} = g_{\mu\nu} + u_\mu u_\nu$ is the projection of the metric on the hypersurface orthogonal to u_μ. In the second equality we used the fact that $u^\nu \nabla_\mu u_\nu = 0$. The

four-velocity field u^μ of the fluid component is a time-like unit vector. Thus, the spatial hypersurfaces orthogonal to u^μ define a foliation of the spacetime. Comparing the equation (4.35) with the definition of the extrinsic curvature (2.12) shows that the expansion tensor is just two times the extrinsic curvature of the spatial hypersurfaces comoving with the fluid component. From the ADM equations (2.16) we can then conclude that it is the expansion tensor that drives the time evolution of the spatial hypersurfaces.

The quantity of interest here, however, is the expansion scalar, which can be obtained without calculating explicitly the components of the expansion tensor:

$$\Theta = g^{\mu\nu}\Theta_{\mu\nu} = \nabla_\alpha u^\alpha = \frac{\partial_\alpha(\sqrt{-g}u^\alpha)}{\sqrt{-g}} = \partial_\alpha u^\alpha + \frac{d\ln\sqrt{-g}}{d\tau}\,, \tag{4.36}$$

where the determinant of the metric g can be written as $\sqrt{-g} \equiv J_T\, J_R\, J_A$, with

$$J_T \equiv \alpha\,, \quad J_R \equiv \frac{\hat{H}_{\theta\theta} + r\hat{H}_{\theta\theta,r}}{\sqrt{1+2E}} \quad \text{and} \quad J_A \equiv r^2\hat{H}^2_{\theta\theta}\sin\theta\,. \tag{4.37}$$

Physically expansion scalar represents the rate of change of infinitesimal volume of the fluid.

We then define the temporal, radial and angular expansion scalars:

$$\begin{aligned}
\Theta_T &\equiv \partial_t u^t + \frac{d\ln J_T}{d\tau} = \frac{r}{\alpha}\gamma^3\dot{\tilde{v}}_p + \frac{\gamma v_p}{H_{rr}}\frac{\alpha_{,r}}{\alpha}\,,\\
\Theta_R &\equiv \partial_r u^r + \frac{d\ln J_R}{d\tau} = \partial_r\left(\frac{\gamma v_p}{H_{rr}}\right) + \gamma\Big(-K^r{}_r + S_R\Big)\,,\\
\Theta_A &\equiv \partial_\theta u^\theta + \partial_\phi u^\phi + \frac{d\ln J_A}{d\tau} = 2\gamma\Big(-K^\theta{}_\theta + S_A\Big)\,,
\end{aligned} \tag{4.38}$$

where we defined:

$$\begin{aligned}
S_R &\equiv v_p\frac{H_{rr,r}}{H_{rr}} = r\tilde{v}\left(\frac{2\hat{H}_{\theta\theta,r} + r\hat{H}_{\theta\theta,rr}}{\hat{H}_{\theta\theta} + r\hat{H}_{\theta\theta,r}} - r\frac{2\tilde{E} + r\tilde{E}}{1+2r^2\tilde{E}}\right), \qquad \text{and}\\
S_A &\equiv v_p\frac{H_{\theta\theta,rr}}{H_{rr}H_{\theta\theta}} = \tilde{v}\frac{\sqrt{1+2r^2\tilde{E}}}{\hat{H}_{\theta\theta}}.
\end{aligned} \tag{4.39}$$

The quantities S_R and S_A can be understood as the radial and angular spatial expansion rates relevant for non-comoving fluids.

Substituting expressions (4.38) into equations (4.34) and (4.36) we eventually get the desired expressions for the acceleration and expansion scalars

$$\begin{aligned} a &= \gamma^2 \frac{dv_p}{d\tau} - r\gamma\tilde{v}K^r{}_r + \frac{\gamma}{H_{rr}}\frac{\alpha_{,r}}{\alpha}, \\ \Theta &= \gamma^2 \frac{dv_p}{d\sigma} - \gamma K + 2\gamma\tilde{v}\frac{\hat{H}_{\theta\theta} + r\hat{H}_{\theta\theta,r}}{H_{rr}\hat{H}_{\theta\theta}} + \frac{\gamma v_p}{H_{rr}}\frac{\alpha_{,r}}{\alpha}. \end{aligned} \tag{4.40}$$

Here we used notation $H_{rr} \equiv (r\hat{H}_{\theta\theta})_{,r}/\sqrt{1+2r^2\tilde{E}}$.

Next we assume that each fluid component satisfies a barotropic equation of state

$$p = w\rho, \tag{4.41}$$

where $w = w(t, r, \rho)$. Now, the true dynamical variables in equations (4.29)-(4.30) are the energy density ρ and the velocity of the fluid v_c. Substituting expressions (4.40) into these equations and manipulating them slightly, we can finally obtain equations for ρ and scaled velocity variable $\tilde{v} \equiv v_p/r$

$$\dot{\tilde{v}} = -\frac{\alpha\left(1-c_s^2\right)\tilde{v}}{H_{rr}\left(1-r^2c_s^2\tilde{v}^2\right)}\left(\tilde{v} + r\tilde{v}_{,r}\right) + \frac{\alpha}{\gamma\left(1-r^2c_s^2\tilde{v}^2\right)}C, \tag{4.42}$$

$$\begin{aligned} \dot{\rho} = &-\frac{\alpha r\tilde{v}}{H_{rr}}\left(1 - \frac{c_s^2}{\gamma^2\left(1-r^2c_s^2\tilde{v}^2\right)}\right)\rho_{,r} + \frac{r^2\tilde{v}^2\dot{w}}{1-r^2c_s^2\tilde{v}^2}\rho + \frac{r\tilde{v}}{H_{rr}}\frac{\alpha w_{,r}}{1-r^2c_s^2\tilde{v}^2}\rho \\ &-\frac{\alpha}{1-r^2c_s^2\tilde{v}^2}D\left(\rho + p\right), \end{aligned} \tag{4.43}$$

where we defined the adiabatic speed of sound

$$c_s^2 \equiv \left(\frac{\partial p}{\partial \rho}\right) \tag{4.44}$$

and furthermore

$$\begin{aligned} C \equiv &\frac{\tilde{v}}{\gamma}\left(K^r{}_r - c_s^2K - \frac{1}{\alpha}\frac{\dot{w}}{1+w} - \frac{1}{H_{rr}}\frac{w_{,r}}{1+w}\right) - \frac{c_s^2}{r\gamma^3H_{rr}}\frac{\rho_{,r}}{\rho+p} \\ &+2\frac{c_s^2\tilde{v}^2}{\gamma}\frac{\sqrt{1+2r^2\tilde{E}}}{\hat{H}_{\theta\theta}} - \frac{1}{r\gamma H_{rr}}\frac{\alpha_{,r}}{\alpha}, \\ D \equiv &\frac{2\tilde{v}}{\hat{H}_{\theta\theta}}\sqrt{1+2r^2\tilde{E}} - K + r^2\tilde{v}^2K^r{}_r + \frac{\left(\tilde{v} + r\tilde{v}_{,r}\right)}{H_{rr}} + \frac{r\tilde{v}}{H_{rr}}\frac{\alpha_{,r}}{\alpha}. \end{aligned} \tag{4.45}$$

Remember that $K^r{}_r$ can be solved as in equation (4.24).

Let us make a couple of observations of the fluid equations. First, identifying the reference-frame velocity $u^\alpha_{\rm rf}$ with the velocity $u^\alpha_{\bar{i}}$ of the $\bar{i}$:th fluid-component we can obtain the rest-frame expressions of Eqs. (4.29-4.30) by simply setting $v_p = 0$:

$$\frac{1}{\alpha}\dot{\rho}_{\bar{i}} = -\Theta_{\rm rf}\left(\rho_{\bar{i}} + p_{\bar{i}}\right), \tag{4.46}$$

$$p'_{\bar{i}} = -a_{r,\,\rm rf}\left(\rho_{\bar{i}} + p_{\bar{i}}\right), \tag{4.47}$$

where $a_{r,\,\rm rf} = \frac{\alpha'}{\alpha}$ and $a_{t,\,\rm rf} = 0$ (see Appendix of paper [II]). The last equation in particular shows that the pressure gradients are the sole cause for non-geodesity.

Second, because of the (twice contracted) Bianchi identity the Einstein tensor is covariantly conserved $\nabla_\mu G^{\mu\nu} = 0$, and we find that

$$\sum_{i=1}^{n} \nabla_\mu T_i^{\mu\nu} = 0\,. \tag{4.48}$$

In the spherically symmetric case the equations with $\nu = t$ and $\nu = r$ are independent. As a result of these constraints, two conservation equations out of the total of $2n$ fluid equations are not independent when considered together with the Einstein equations. This just clarifies why the constraint equations could be left out of the set.

4.3 Dust Frame

In all models of interest for us we have at least one dust component. In these cases we can choose the coordinate system comoving with the dust. Since dust has a vanishing pressure, the dust frame coincides with the geodesic slicing $\alpha \equiv 1$, in addition to requirement that the radial velocity field of the dust component vanishes. This can also be seen from equation (4.43) by writing K in terms of $\hat{H}_{\theta\theta}$, H_{rr} and their time derivatives. In this case the energy density of the dust ρ_M can be solved analytically in terms of the metric variables, yielding

$$\rho_M = \bar{\rho}_M \frac{\bar{\hat{H}}^2_{\theta\theta}\bar{H}_{rr}}{\hat{H}^2_{\theta\theta}H_{rr}}. \tag{4.49}$$

Here the overbar denotes the initial-value profile.

Now, consider a model where we have a dust component and n perfect-fluid components with equations of state $p_i = w_i\rho_i$, where $w_i = w_i(t, r, \rho_i)$ and $i = 1, ..., n$. Choosing the dust frame coordinate system as defined above, we find a complete system of equations for the variables $\hat{H}_{\theta\theta}$, $K^r{}_r$, $\tilde{E}$, $\{\tilde{v}_i\}_{i=1}^n$ and $\{\rho_i\}_{i=1}^n$ as follows:

$$
\begin{aligned}
\dot{\hat{H}}_{\theta\theta} &= -\hat{H}_{\theta\theta}K^r{}_r, \\
\dot{K}^\theta{}_\theta &= -\frac{\tilde{E}}{\hat{H}^2_{\theta\theta}} + \frac{3}{2}\left(K^\theta{}_\theta\right)^2 + \frac{1}{2}\sum_{i=1}^{n}\gamma_i^2\left(r^2\tilde{v}_i^2 + w_i\right)\rho_i, \\
\dot{\tilde{E}} &= \frac{1}{2}\hat{H}_{\theta\theta}\sqrt{1+2r^2\tilde{E}}\sum_{i=1}^{n}\gamma_i^2\tilde{v}_i\left(1+w_i\right)\rho_i, \\
\dot{\tilde{v}}_i &= -\frac{\left(1-c_{s,i}^2\right)\tilde{v}_i}{H_{rr}\left(1-r^2c_{s,i}^2\tilde{v}_i^2\right)}\left(\tilde{v}_i + r\tilde{v}_{i,r}\right) + \frac{1}{\gamma\left(1-r^2c_{s,i}^2\tilde{v}_i^2\right)}C, \qquad (4.50) \\
\dot{\rho}_i &= -\frac{r\tilde{v}_i}{H_{rr}}\left(1 - \frac{c_{s,i}^2}{\gamma^2\left(1-r^2c_{s,i}^2\tilde{v}_i^2\right)}\right)\rho_{i,r} + \frac{r^2\tilde{v}_i^2\dot{w}}{1-r^2c_{s,i}^2\tilde{v}_i^2}\rho \\
&\quad + \frac{r\tilde{v}_i}{H_{rr}}\frac{w_{i,r}}{1-r^2c_s^2\tilde{v}_i^2}\rho_i - \frac{1}{1-r^2c_{s,i}^2\tilde{v}_i^2}D\left(1+w_i\right)\rho_i, \qquad (4.51)
\end{aligned}
$$

where definitions for C and D are given in Eq. (4.45). These equations form a complete set of nonsingular, well behaved equations for numerical applications

4.4 Initial Values and Boundary Conditions

The initial conditions for the curvature fuction $\bar{E} \equiv E(\bar{t}, r)$ in the multi-component model can be set to correspond to simultaneous big-bang singularity in the coordinate time. This condition ensures that there are no decaying modes. As long as the initial conditions are given well after inflation, non-negligible decay modes would have had to be of enormous size at the onset of inflation. For this reason decay modes are considered to conflict with the inflationary paradigm [85]. In our current variables the equation for vanishing bang-time function is (see Eq. (2.37) of paper [II]):

$$
\bar{t} = \int_0^{\bar{t}} dt \frac{\dot{H}_{\theta\theta}}{\alpha\sqrt{\frac{F}{4\pi H_{\theta\theta}} + 2r^2\tilde{E}}}. \qquad (4.52)
$$

Here a problem is that the lapse α, the effective gravitational mass F and the curvature function E depend on the time coordinate. In the pure LTB model they

are time independent and thus the integration variable can be easily changed to $H_{\theta\theta}$. However, if we consider lapseless gauge $\alpha \equiv 1$, and a model with constant equation of state parameters w_i and specify initial conditions at sufficiently early times $\bar{t}$, such that the size of the inhomogeneity is much larger than the causal horizon (the pressure gradients can be neglected), the evolution of causal patches effectively followed an FLRW model before $\bar{t}$, approximately setting $E(t,r) = \bar{E}$ before $\bar{t}$. This observation gives the scaling relations for individual components, so that by equation (2.26) we can approximate the time dependence of F as

$$F \approx \sum_{i=1}^{n} \left(\frac{\bar{H}_{\theta\theta}}{H_{\theta\theta}}\right)^{3w_i} \bar{F}_i, \tag{4.53}$$

where $\bar{F}_i$ is the initial profile for the i:th component gravitating mass. While there is no really meaningful division into components for the gravitating mass in general, such division is useful prescription for the initial gravitating mass.

Using Eq. (4.53) and making the change of variables $H_{\theta\theta} \longrightarrow \tilde{y} \equiv \frac{H_{\theta\theta}}{\bar{H}_{\theta\theta}}$ in the integral of Eq. (4.52) then yields

$$\sqrt{\frac{\bar{F}}{4\pi\bar{H}_{\theta\theta}^3}}\bar{t} \approx \int_0^1 d\tilde{y} \frac{1}{\sqrt{\sum_{i=1}^{n} \tilde{y}^{-3w_i-1}\frac{\bar{F}_i}{\bar{F}} + \frac{8\pi\bar{H}_{\theta\theta}\bar{E}}{\bar{F}}}}. \tag{4.54}$$

For a flat FLRW background metric effective gravitating mass would be

$$F_{\text{bkg}} = 4\pi\bar{H}^2(r\bar{a})^3 \sum_{i=1}^{n} \bar{\Omega}_i \left(\frac{\bar{a}}{a}\right)^{3w_i}, \tag{4.55}$$

where $\bar{\Omega}_i$ is the background energy density of the i:th component in units of the critical density ρ_{cr} and $\bar{H}$ the Hubble rate at $\bar{t}$. Clearly we have $\bar{F}_{\text{bkg}} = 4\pi\bar{H}^2(r\bar{a})^3$. Next we fix the r coordinate so that $\bar{H}_{\theta\theta} \equiv r\bar{a}$ and choose to work with such initial density profiles that effectively $\bar{F}_i \approx \bar{\Omega}_i\bar{F}$. Note here that when $i \neq 1$ the factor $\bar{\Omega}_i$ should actually have r dependence, but its effect on the integral would be negligible. We also observe that by definition in the background model:

$$\bar{H}\bar{t} \equiv \int_0^1 d\tilde{y} \frac{1}{\sqrt{\sum_{i=1}^{n} \bar{\Omega}_i\tilde{y}^{-3w_i-1}}} \equiv I_{1/2}. \tag{4.56}$$

Then, expanding (4.54) around $\frac{8\pi\bar{H}_{\theta\theta}\bar{E}}{\bar{F}} = 0$, using (4.56) we find that to the

lowest order in $\bar{\delta}_{\bar{F}} \equiv \frac{\bar{F}}{\bar{F}_{\rm bkg}} - 1$:

$$\bar{E} \approx -\frac{1}{2}\left(r\bar{a}\bar{H}\right)^2 \frac{I_{1/2}}{I_{3/2}}\bar{\delta}_{\bar{F}}, \tag{4.57}$$

where

$$I_{3/2} \equiv \int_0^1 d\tilde{y} \frac{1}{\left(\sum_{i=1}^n \bar{\Omega}_i \tilde{y}^{-3w_i-1}\right)^{3/2}}. \tag{4.58}$$

This result is a generalization of the result of Ref. [86] for the LTB model which was used in the papers [II] and [III] where the initial conditions were set during matter domination. Indeed, in the pure dust case Eq. (4.57) clearly reduces to the result

$$\bar{E}(r) = -\frac{5}{6}(r\bar{a}H_{out})^2\bar{\delta}_{F_M}(r). \tag{4.59}$$

For a comparison, in the pure radiation case (i.e. $w = \frac{1}{3}$) we find instead

$$\bar{E}(r) = -\frac{1}{6}(r\bar{a}H_{out})^2\bar{\delta}_{F_{\rm rad}}(r). \tag{4.60}$$

The initial condition for the dust and radiation case can also be integrated analytically. We find

$$\bar{E}(r) = \frac{5}{3}r^2\bar{\Omega}_M^2 \frac{3\bar{\Omega}_M - 2 + 2\bar{\Omega}_R^{3/2}}{16\left(1-\bar{\Omega}_R^{5/2}\right)}\bar{\delta}_F(r), \tag{4.61}$$

where $\bar{\Omega}_M + \bar{\Omega}_R \equiv 1$

4.5 Effective FLRW Model at Early Times

The acoustic oscillation features seen in the CMB spectrum are supposed to have arisen from the gravitational instabilities seeded by the primordial fluctuations. At that time the universe effectively looked like a linearly perturbed FLRW model so that inhomogeneous models may be embedded in an FLRW background independently of the acoustic oscillations. As a result the local inhomogeneous structure only affects the high-multipole end of the CMB spectrum through the distance to the recombination surface [20]. However, for a real inhomogeneity

its geometry would most likely dominate the low multipoles. As a result the low multipoles in the spectrum are really not meaningful quantities in spherically symmetric local models. Because the inhomogeneity distorts the observed local Hubble rate and thereby the temperature of the CMB compared to an observer in the background FLRW universe, the present-day values of cosmological parameters of the two must be related before the results for the acoustic peaks in an FLRW background can be used to constrain the model.

Studies of spherically symmetric large-scale inhomogeneities have been based on the assumption that radiation does not have to be included to the actual inhomogeneous source. The distances of the inhomogeneous model and the effective FLRW background with radiation can be matched during the matter domination and well beyond the actual inhomogeneity scale. Effects of the weak radiation background on the cosmic evolution are expected to be negligible after that particular redshift. Due to the different expansion rates within the inhomogeneity, the present-day CMB temperature in the FLRW background differs from the observed value. See section 3 of paper [I] for more details on determining the effective FLRW model. However, it is not conclusively clear *a priori* how the initial conditions for the baryonic component at recombination should be set. This is due to pre-recombination plasma phase of the baryonic matter which has not been modelled in the context of exact inhomogeneous models.

5 Cosmological Applications

In this section we go through the results of papers [I]-[III]. In paper [I] we directly compared ΛCDM and local-void models by extending the pure dust LTB model in to same parameter space with ΛCDM by inclusion of the cosmological constant. This way the ambiguities in the number of degrees of freedom associated with the likelihood comparison were removed. In addition to comparison of the two scenarios, this also allowed to study how a mixed scenario would affect the determination of cosmological parameters. In paper [II] we studied more general spherically symmetric models sourced by multitude of perfect fluid components with arbitrary equations of state. We were able to present the dynamical equations in compact and tractable form, but were faced with difficulties with numerical implementation for more general equations of state. These difficulties were confronted with the ADM formalism in previous section. However, we found an interesting fluid model with negative pressure and without pressure gradients. This model, which depicts dark energy with zero sound speed, turned out to be numerically easily manageable. This model allowed to study how local

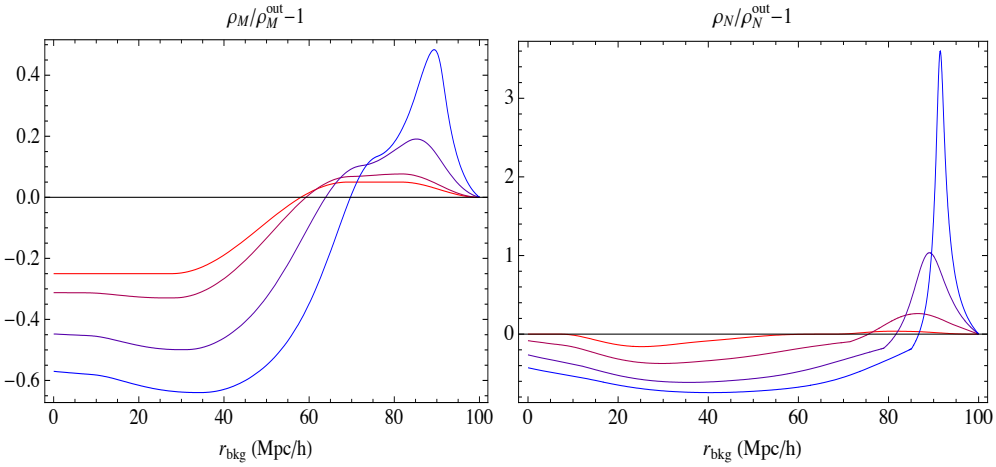

Figure 9: Evolution of the contrasts of M component energy density (left panel) and N component energy density (right panel) for z =5 (red), 3, 1 and 0 (blue). Figure is from paper [II]

large-scale inhomogeneities would affect our perception of the equation of state for dark energy which was the subject of paper [III].

Other studies on spherically symmetric multi-component fluids have concentrated on the case with dust and radiation. Reference [22] presented the necessary equations linearized in the relative verlocity. However, the authors did not analyze the solution to these equations in any detail. The case with dust and radiation was studied with a succesful numerical implementation for initially superhorizon inhomogeneities in [87]. However, they only presented a scheme for numerical implementation and left further applications for future work.

All models studied in this section use the homogeneous big-bang condition (4.59), which guarantees vanishing decay modes. Models with an inhomogenous bang-time function were studied in [21] in the context of the local void explanation for the dark energy. This was done to find out if allowing decay modes would relax the difficulties with satisfying all the observational constraints in pure dust void models. They found out that there was no significant improvement to be achieved, but left open the possibility for having non-negligible effects by including the radiation when modelling the early evolution of an inhomogeneity.

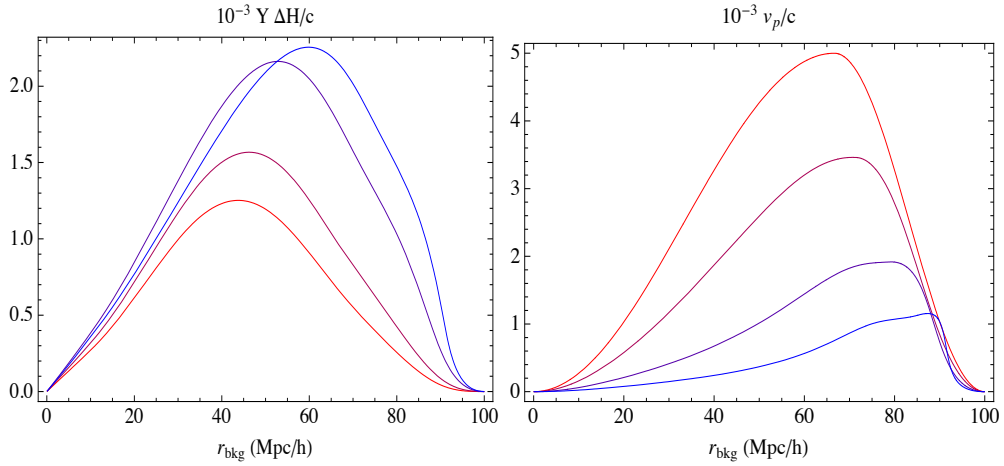

Figure 10: Left panel: evolution of the velocities relative to the background $v_M \equiv -H_{\theta\theta}(K^{\theta}{}_{\theta,\mathrm{out}} - K^{\theta}{}_{\theta}) = Y\Delta H/c$ of the M component for z =5 (red), 3, 1 and 0 (blue). Right panel: evolution of the proper velocities of the N component with respect to the M component for z =5 (red), 3, 1 and 0 (blue). Figure is from paper [II]

5.1 Non-comoving dust

In the post-recombination evolution the standard model has essentially two dust-components: baryonic and cold dark matter. Dust is, by definition, in geodetic motion, so if initially two dust components are in rest with respect to each other, they will not develop velocities with respect to each other later during the evolution. However, the fact that CDM decoupled before baryons introduces a difference in their perturbed densities. Thus, they should be described as two non-comoving dust components from the epoch of the last scattering onwards until baryons fall in to CDM potential wells. The delayed decoupling of baryons results from the pressure in the photon-baryon plasma, when gradients push the baryonic inhomogeneities away from the geodetic flow and initially prevents baryonic matter from falling into the gravitational potential wells associated with the CDM distribution.

The nonlinear relativistic evolution of inhomogeneities in a dust-baryonic-plasma would be interesting. Under the spherically symmetric prior, this can be done using the formalism presented in the previous section. This would allow to study non-comoving dust inhomogeneities with realistic initial relative velocity profiles. In the case studied in paper [II], which we present here, the initial profile was rather arbitrarily chosen.

Figures 9 and 10 illustrate the case of an underdensity with two non-comoving dust components in a standard ΛCDM background. The subscript M refers to the rest-frame dust component and N to the dust component with initially non-vanishing relative velocity. In figure 9 we see evolution of local density contrasts δ_M and δ_N. The figure shows how the evolution of the non-comoving component induces a feature on the rest-frame components profile. Both the density contrasts show a realistic evolution, with overdense regions contracting and becoming thin shells (mimicking structures), and underdense regions becoming larger and deeper (mimicking voids). Note in particular how the N component induces gravitationally a peak in the density of the M component. In figure 10 we see the evolution of local velocities associated with the two components. Velocities are seen by an observer situated in the background for the rest-frame component(left panel), and relative proper velocities v_p for the non-comoving component (right panel). We can see that the velocities relative to the background increase as the underdensity gets emptier. On the other hand, the gravitational attraction between the two components reduces their relative velocities v_p. The redshifts in the figures are relative to the background solution.

5.2 ΛLTB model

The pure dust solution, i.e. LTB model which is exactly solvable, can easily be extended with a non-vanishing cosmological constant. In this case the model is still exactly solvable, and the solution can be represented in terms of elliptic integrals [91]. With a non-vanishing cosmological constant the LTB model is effectively extended into the same parameter space with the ΛCDM model when the early evolution is understood in terms of the effective metric. This allows to make a direct comparison between the ΛCDM and the local-void model. In particular the model allows to find out if there are degeneracies between the value of cosmological constant and dimensions of a local inhomogeneity.

This was done in paper [I]. We compared the models with standard χ^2-likelihood analysis in the parameter space consisting of seven parameters. Parameters which specify the FLRW background model, are background curvature density $\Omega_{K,\mathrm{out}}$, DE density $\Omega_{\Lambda,\mathrm{out}}$, present age of the universe t_0 and the spectral index n_s, respectively. Parameters $\Omega_{M,\mathrm{in}}$, r_0 and Δr, which specify the void dimensions, are free parameters associated with the chosen dust density profile

$$\Omega_M(r) = \Omega_{M,\mathrm{out}} - (\Omega_{M,\mathrm{out}} - \Omega_{M,\mathrm{in}}) \frac{1 - \tanh\left((r - r_0)/(2\Delta r)\right)}{\tanh\left(2\Delta r\right)}, \tag{5.1}$$

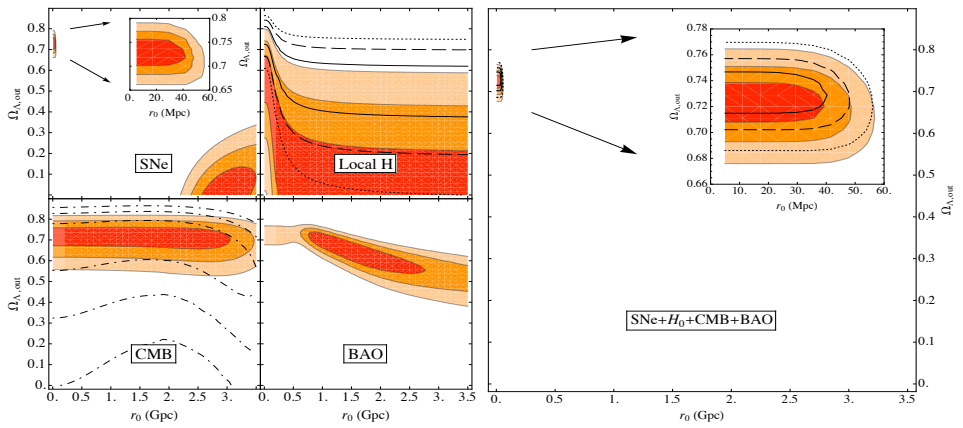

Figure 11: Shown are the 1, 2 and 3σ confidence level contours on r_0 and $\Omega_{\Lambda,\mathrm{out}}$ for the likelihood for the ΛLTB model with $n_s = 0.96$, $t_0 = 13.7$ Gyr and $\Omega_{K,\mathrm{out}} = 0$. On the left, the smaller panels show the contours for the independent likelihoods per observable (supernovae, local Hubble rate, CMB and BAO). On the right, the larger panel shows the contours for the combined likelihood. In the panel representing measurements of the local Hubble constant, the results relative to H_{S06} are shown as filled contours, and the ones relative to H_{R09} are indicated by black lines. The same labeling holds for the panel relative to the combined observables. In the panel with CMB contraints the dot-dashed contours denote confidence levels for the likelihood marginalized over n_s. Figure is from paper [I].

where $\Omega_{M,\mathrm{out}} = 1 - \Omega_{K,\mathrm{out}} - \Omega_{\Lambda,\mathrm{out}}$.

Figure 11 shows the likelihood contours in planes of the background Ω_Λ and void radius r_0, both for individual observables and combined. We assumed $n_s = 0.96$, $t_0 = 13.7$ Gyr and $\Omega_{K,\mathrm{out}} = 0$ for the background. For the void we assumed $\delta_\Omega \equiv (\Omega_{M,\mathrm{in}} - \Omega_{M,\mathrm{out}})/\Omega_{M,\mathrm{out}} = -0.9$ and $\Delta r = 0.35 r_0$ in order to have good fits with the supernova data. It is evident from the supernova likelihoods that in order for the void to explain away the cosmological constant the void would have to be almost the size of observable universe. However, this conclusion is clearly not relevant under these priors when accounting for the other observables. Likelihoods are shown for two results for the local Hubble rate $H_{\mathrm{S06}} = 62.3 \pm 5.2$ km s^{-1}Mpc^{-1} [62] and $H_{\mathrm{R09}} = 74.2 \pm 3.6$ km s^{-1}Mpc^{-1} [63]. For the CMB constraints, the confidence levels are plotted also with the spectral index n_s marginalized over. This has a strong effect of widening and bending the contours towards the pure-void region. On the other hand, the more accurate determination for the local Hubble rate H_{R09}, which is plotted with black dashed lines in the figure, shifts the confidence levels towards higher $\Omega_{\Lambda,\mathrm{out}}$ due to its higher value.

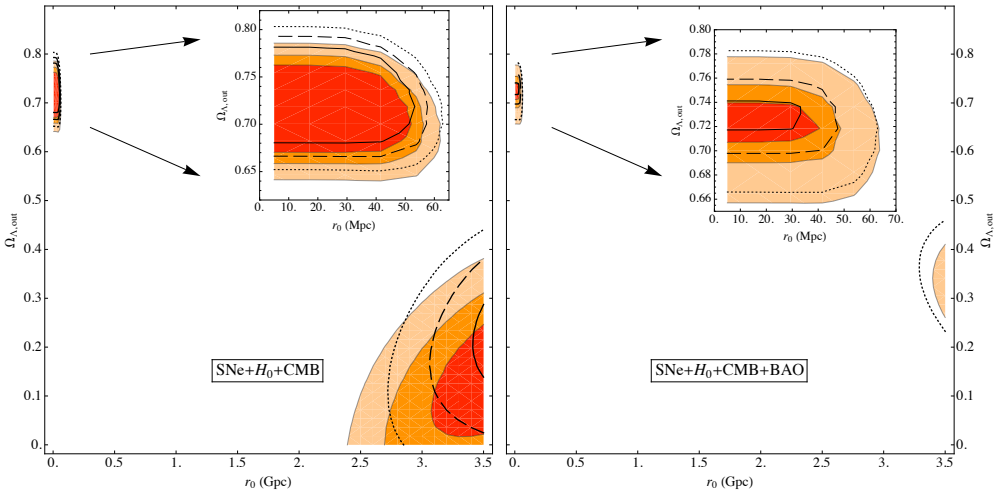

Figure 12: 1, 2 and 3σ confidence level contours on r_0 and $\Omega_{\Lambda,\mathrm{out}}$ for the ΛLTB model with parameters n_s and t_0 and with $\Omega_{K,\mathrm{out}}$ marginalized over. Labelling and definitions as in Fig. 11. Figure is from paper [I]

Figure 12 shows also the confidence-level contours in r_0 and $\Omega_{\Lambda,\mathrm{out}}$ plane for the ΛLTB model. Priors for the void dimensions are the same. However, here the spectral index, age of the universe and the background FLRW model spatial curvature $\Omega_{K,\mathrm{out}}$ are marginalized over. Clearly, including BAO data excludes the void models with the profile of Eq. (5.1). However, as was shown in [17] the transversal BAO data can always be accommodated by fine tuning the density profile. It is also appropriate to note that the BAO scale is a perturbative quantity and the perturbation theory for the LTB metric is not fully developed yet. It is therefore reasonable to do the analysis also excluding the BAO constraints. In comparison to Fig. (11) the marginalization and exclusion of the BAO constraint brought a local likelihood minimum on the pure-void axis below the confidence-levels bringing a simple void model superficially on par with the concordance ΛCDM model. This effect is partly explained by the relaxation of the CMB constraints with the prior for the spectral index n_s as illustrated already in the figure 11. The background curvature has significant impact on the area distance to the last-scattering surface while also modifying the shape of the luminosity distance-redshift relation. The age of the universe on the other hand, essentially sets the local Hubble rate. Interplay between these effects is what allows to find void models that are in better agreement with the data. However, the figure shows the difficulties with accommodating a higher value for the local Hubble rate: the most reliable determination H_{R09} already excludes a pure void model on 2σ-level.

In the CMB anisotropy spectrum analysis we used only the positions of the first, second and third peaks and the first through computed from the fitting functions of Ref. [92]. It should be noted that the actual CMB constraints are somewhat tighter. Also the parameter Δr was not marginalized over. This was considered natural because it was found out that the observables were quite insensitive to changes in this parameter. Other variables than BAO are also insensitive to the actual shape of the profile [17], so that the specific choice of Eq. (5.1) should not significantly draw back from generality of the results in this regard. LTB model with the cosmological constant was studied also e.g. in [88], [89], [90].

5.3 Dark energy with negligible sound speed

5.3.1 Model

Let us now study a generalization of the ΛLTB model. In ΛCDM the cosmological constant with its equation of state $w \equiv -1$ is a prior. Therefore it is interesting to study how local large-scale inhomogeneities would affect our intepretation of cosmological observations if the prior $w \equiv -1$ is relaxed. To this end we first define the adiabatic sound speed in a fluid

$$c_s^2 \equiv \left(\frac{\partial p}{\partial \rho}\right)_s, \tag{5.2}$$

where ρ and p are fluid energy and pressure densities respectively. The subscript s refers to the adiabatic condition of keeping the entropy density constant. Clearly a vanishing adiabatic sound speed for a fluid means that there are no pressure gradients which is trivially true for dust.

Let us now consider the class of models considered in paper [II]. These models are defined by two components: a dust component and a DE component with equation of state

$$p_w(t,r) \equiv w_0 \left(\frac{\rho_w(t,r)}{\rho_{w,\mathrm{bkg}}(t)}\right)^{\alpha-1} \rho_w(t,r). \tag{5.3}$$

Here w_0 is the constant FLRW background DE equation-of-state parameter and $\rho_{w,\mathrm{bkg}}(t)$ is the background DE density. Clearly, taking $\alpha = 0$ yields homogeneous pressure.

In figures 13 and 14 we have the evolution of dust and DE density contrasts for model with initial (at redshift $z = 1000$) dust density contrast $\delta_M = 1.5 \times 10^{-3}$,

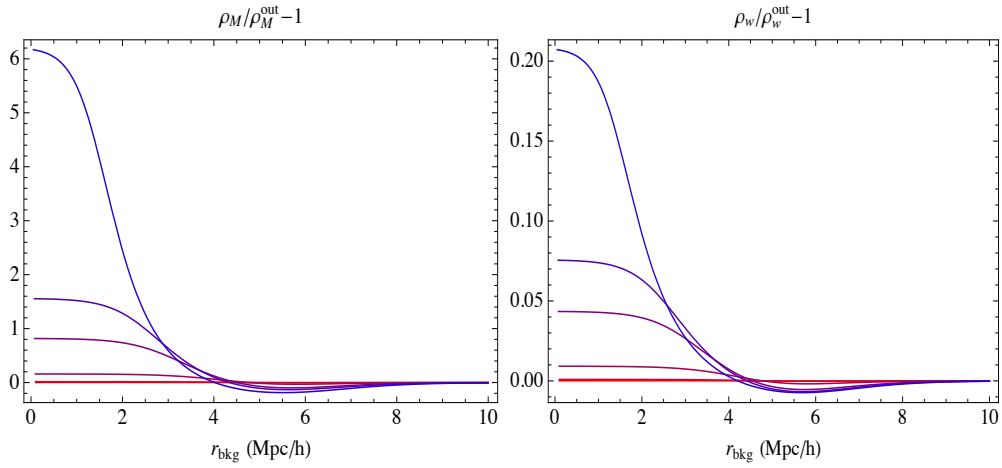

Figure 13: Evolution of the dust component energy density (left panel) and DE component energy density (right panel) in the case with $c_s = 0$ ($\alpha = 0$) for z =1000 (red), 100, 10, 2, 1 and 0 (blue). Figure is from paper [II]

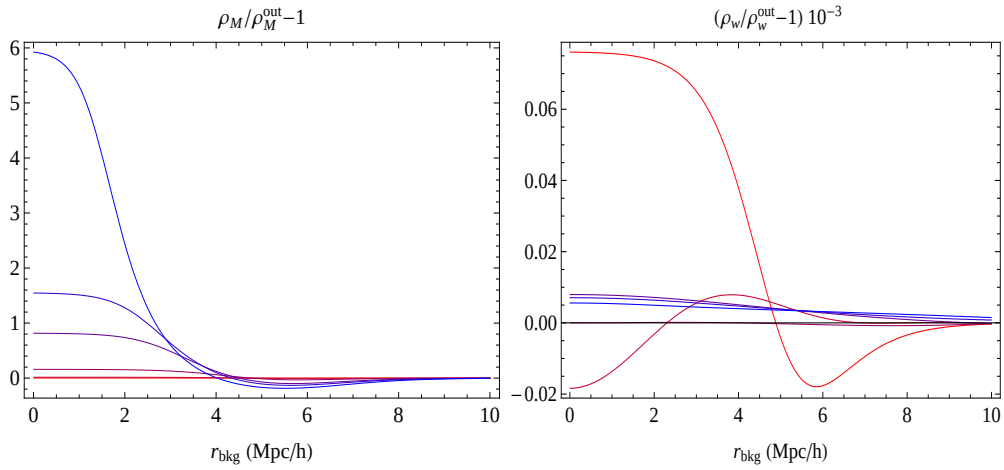

Figure 14: Evolution of the contrasts of M component energy density (left panel) and N component energy density (right panel) in the case with $c_s \approx 0.4c$ ($\alpha = -0.2$) for z =1000 (red), 100, 10, 2, 1 and 0 (blue).

$r_0 = 10$ Mpc$/h$ and $\Delta r = 0.3 r_0$. The DE component is initially at rest with respect to dust and initial singularity is set to simultaneous by Eq. (4.59). The flat background model is set by equation-of-state parameter $w_0 = -0.8$, dimensionless Hubble parameter $h = 0.7$ and dimensionless present-day dust density $\Omega_M = 0.3$. In figure 13 $\alpha = 0$ giving the case with vanishing sound speed used in the analysis of section 5.3.2. In figure 14, on the other hand, we have $\alpha = -0.2$, which corresponds to $c_s = 0.4$ in units of light speed. In the case with zero sound speed the DE inhomogeneity grows because there are no pressure gradients to drive the fluid into relative motion. With appriciable sound speed, however, the initial inhomogeneity is quickly flattened towards the background density by the pressure. The effect on the final dust density contrast is roughly 5% and apart from the relative velocity, evolution of other variables remain practically unaltered between the two cases. This result shows that, atleast within this class of models, relaxing the prior $c_s = 0$ for the DE component does not alter the results of paper [III] summarized in section 5.3.2. Also the amplitude of the DE inhomogeneity is so small for plausible models that the sound speed is not expected affect those same results.

Models with DE equation of state (5.3) were studied in paper [II]. However, we confronted numerical problems with non-negligible sound speeds. We were able to have results only up to $\alpha \approx 10^{-10}$ for the case studied above. Figure 14 is previously unpublished result and illustrates the fact that the new set of equations (4.51) derived here really is numerically more manageable.

5.3.2 Likelihood Analysis

A dark-fluid component with vanishing speed of sound can be modelled by requiring that there are no pressure gradients. That is $p_w = p_w(t) = w_{\text{out}} \rho_{w,bkg}(t)$, corresponding to the special case $\alpha = 0$ in Eq. (5.3), where $\rho_{w,bkg}(t)$ is the FLRW-background energy density of the dark fluid and $w_{\text{out}} < -\frac{1}{3}$ the constant equation of state parameter. Clearly for $w_{\text{out}} = -1$ and a homogeneous initial dark-fluid density the cosmological constant is recovered. Thus the model with such dark-fluid and dust components embedded in an FLRW background is a generalisation of the ΛLTB model of the present section. Where the ΛLTB model allowed to look for degeneracies between the value of the cosmological constant and the dimensions of a local inhomogeneity, the generalized model allows to look for degeneracies also between the e.o.s. parameter (of the particular model) and dimensions of a local inhomogeneity. Crossing the phantom line (i.e. for $w_{\text{out}} < -1$) makes an underdensity in the dust component correspond to an overdensity in the dark-energy component and similarily an overdensity to cor-

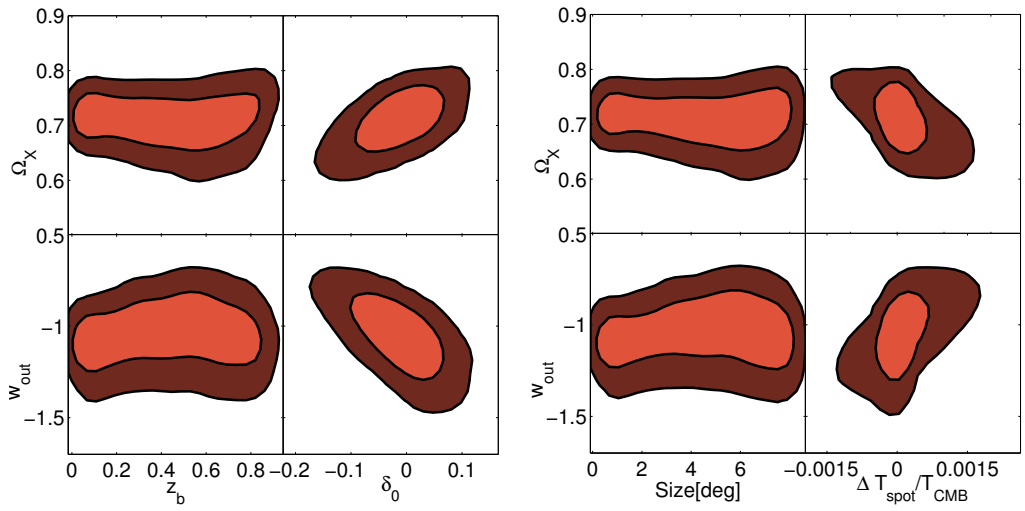

Figure 15: Two-dimensional marginalized 1 and 2σ confidence-level contours for the most interesting parameters characterizing the cosmological model endowed with a local inhomogeneity. The left and right figures show the same information. However, on the right panel z_b and δ_0 are traded in for the angular diameter that the inhomogeneity would have if it were located at the observer's last scattering surface and the temperature fluctuation that it would induce, respectively. Figure is from paper [III]

respond to an underdensity [II]. This can be understood by looking at the fluid equation (4.43): for dust in its rest-frame, the sign of $\dot{\rho}$ is determined by the sign of K. Clearly, for phantom-like DE, initially at rest (i.e. $\tilde{v} = 0$), the sign of $\dot{\rho}$ is just the opposite since in this case $\rho + p \propto -\rho$.

Figure 15 shows the two-dimensional marginalized posterior probability distributions for the background dark-energy density Ω_X and the size of the inhomogeneity, expected by the redshift to the boundary of the inhomogeneity z_b and the density contrast δ_0, as well as for the equation-of-state parameter w_{out} and inhomogeneity dimensions. Parameters are constrained by the Union 2 compilation for supernovae [70], the WMAP 7-year results for CMB [93] and the Hubble rate of Eq. (3.3). While the model is rather specific, any appreciable degeneracy would serve the purpose to point out that such scenario would twist our perception of the dark energy when naively interpreting the observations within the context of FLRW cosmology. Since the inhomogeneities of opposite signs have opposing effects, marginalizing over the amplitudes mostly widens the tails for distributions over Ω_X and w_{out}. This result (Fig. 4 in [III]) estimates how inhomogeneities contribute to the error budget when determining the cosmological parameters.

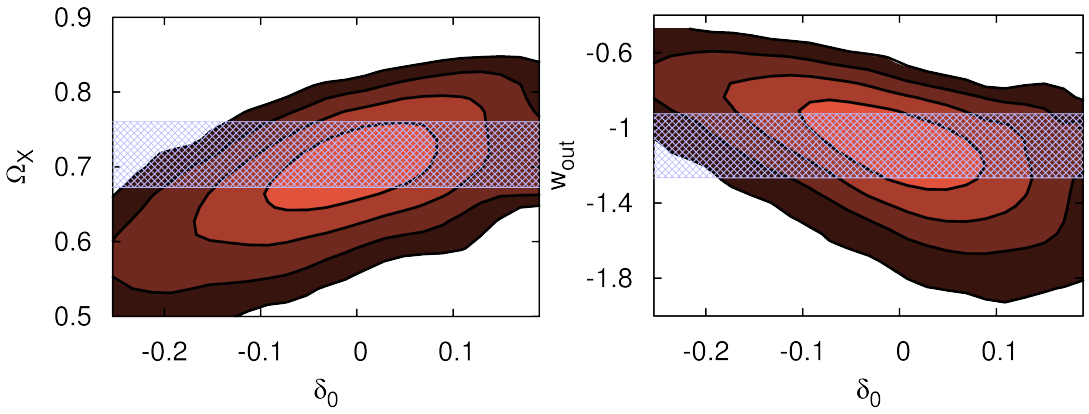

Figure 16: Two-dimensional 1, 2, 3 and 4σ confidence-level contours for Ω_X and $w_{\rm out}$ with δ_0, constrained by CMB, SNe, and H_0. The horizontal band corresponds to the one-dimensional 2σ c.l. constraints on Ω_X and $w_{\rm out}$ for the wCDM FLRW model. Figure is from paper [III]

In figure 16 we have likelihoods on (Ω_X, δ_0)- and (w_0, δ_0)-planes, marginalized over other parameters, together with the 2σ contours for corresponding homogeneous models. This plot shows that if future data will constrain $|\delta_0|$ to be large, then the inclusion of such data will shift the best fit region towards values of w that are far from -1. Clearly, a local inhomogeneity of order $|\delta_0| \approx 0.1$ would shift the best-fit region to disfavor the cosmological constant.

Figure 17 shows the CMB dipoles for an observer situated away from origin, inside an inhomogeneity of 1 Gpc radius. On the right vertical axis the corresponding peculiar velocity, which is derived assuming that the observed CMB dipole is caused solely by the peculiar velocity of the observer, is listed. The magnitude of the velocities does not exceed the magnitude of expected random velocities. The effect does not go to zero outside the LTB patch due to the integrated Sachs-Wolfe effect induced by the LTB structure. Both cases shown in the figure are for models with particular parameters to give appreciable deviation from the ΛCDM. However, the peculiar velocities induced are within the limits of the observed dipole. Since the observed CMB dipole anisotropy is of order $\Delta T/T \propto 10^{-3}$ the analysis suggests that Gpc scale structures with $\delta_0 \propto 0.1$ are not excluded by present observations. For further details on how the figures were obtained see section 4.2 in paper [III].

The probability for existence of an inhomogeneity of a given type around a given point in space, can be approximately drawn from the almost scale-invariant power spectrum set by the CMB observations (assuming that it is of the same primordial

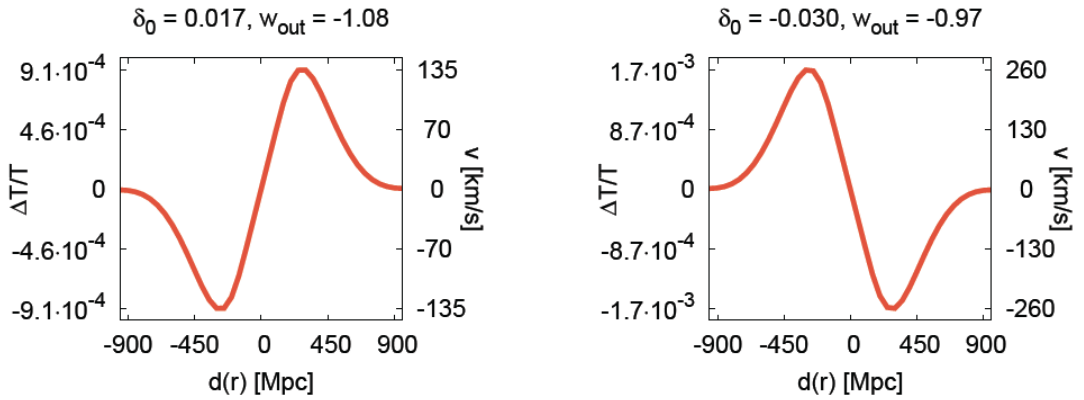

Figure 17: The CMB-dipole observed by observers at different radii $d(r)$ in an LTB patch with a radius of 1 Gpc, for an over-density (left) and an under-density (right). Figure is from paper [III]

origin of course) [III]. In general drawing the probabilities is complicated due to these probabilities being conditional to the structures not residing within larger structures. However, since in the present case the scales of inhomogeneities are so large, this can be done in a straightforward manner neglecting these cloud-in-cloud, void-in-void and void-in-cloud effects. In [III] it was found that for models with appreciable deviation from the standard model, the probability can be up to three times the dispersion of the smoothed density field, corresponding to almost percent level probabilities, associated with the CMB spectrum. For further details see section 4.5 of [III].

6 Discussion

In this thesis we have illustrated the uncertainties related to the so-called precision cosmology due to our incomplete knowledge of our cosmic neighbourhood. In particular, we have employed a series of spherically symmetric models of varying complexity in order to address this problem. We wrote the equations of paper [II] for a spherically symmetric metric sourced by n perfect fluid components with indeterminate equations of state using the ADM formalism. Furthermore, we identified numerically problematic terms in the resulting equations and were able to handle these by introducing more convenient variables. Doing this we ended up with numerically more manageable set of equations than the one presented in paper [II]. Moreover, we derived an approximation for initial conditions

corresponding to simultaneous initial singularity for initially super-Hubble inhomogeneities. These were unpublished results.

We studied the local-void scenario for dark energy by comparing the standard model with local-void models using the LTB model with a cosmological constant. The supernovae, Hubble rate, CMB and BAO data was analyzed by marginalizing the total likelihood over the spectral index, the age of the universe (which essentially sets the local Hubble rate) and the present-day spatial curvature of the FLRW background. The choice of the degrees of freedom for the reduced χ^2 is neccessarily somewhat subjective since the LTB model is specified not by free parameters, but by free functions. The analysis for the ΛLTB model provided a democratic comparison between the standard model and the local-void scenario by setting them within the same parameter space. While these simple void models can accommodate the major observational features suprisingly well, the requirements for the actual nature of the structure leaves a lot to hope for; in order for the underdensity to explain away the need for the cosmological constant it would have to be very deep and have a radius of several Gpc's. Furthermore, the isotropy of the CMB would require that we happen to live very near the center of the void, or we should happen to have a suitable peculiar motion towards the center, which would give rise to a new type of fine-tuning problem in these models. The initial conditions for such enormous structure would require very large peculiar velocities at early times, which would appear incompatible with inflationary physics, and plausible birth mechanisms for such structures remain unknown. Observations on the kSZ-effect, set bounds on the peculiar velocities at the wall of such a void. These bounds also severily constrain spherically symmetric dust solutions as a viable explanation for the dark-energy observations [24], [71]. However, it should be noted that spherical symmetry and smooth continuous matter distribution are major simplifications, and for these reasons the constraint based on the spherically symmetric model should be regarded with some caution.

Results show that existence of local unvirialized structures of dimensions similar to the largest observed structures in the universe could significantly alter the quantitative intepretation of the observational data used to set constraints on the cosmic parameters. For ΛLTB models there was no degeneracy found between the void radii' and the value of the cosmological constant. However, there was an interesting degeneracy found between the background dark-energy-equation-of-state parameter and the inhomogeneity radius in models with vanishing speed of sound (vanishing pressure gradient) of the inhomogeneous dark fluid. In particular, it was found out that local large-scale deviations from statistical homogeneity of inflationary origin could significantly alter our interpration of cosmological ob-

servations in regards to the nature of dark energy. Results of [III] shows (as in Fig. 16) that with prior knowledge on the local inhomogeneity, due to new data from a future survey, it could be possible to rule out the cosmological constant. Vice versa, a hypothetical future data, ruling out the cosmological constant in an FLRW universe, also could still be explained with a local inhomogeneity.

As the modelling and future data gets more and more precise, the uncertainty due to large-scale structure becomes more and more important. Analysis presented in this thesis is just a step towards more accurate reconstruction of realistic cosmology. Anyway, already the results obtained in this thesis show that even the talk about present-day percent-level precision cosmology might certainly be just too optimistic.

References

[1] P. A. R. Ade *et al.* [Planck Collaboration], arXiv:1303.5062 [astro-ph.CO].

[2] C. P. Ahn *et al.* [SDSS Collaboration], arXiv:1307.7735 [astro-ph.IM].

[3] S. Cole *et al.* [2dFGRS Collaboration], Mon. Not. Roy. Astron. Soc. **362** (2005) 505 [astro-ph/0501174].

[4] J. Frieman, M. Turner and D. Huterer, Ann. Rev. Astron. Astrophys. **46** (2008) 385 [arXiv:0803.0982 [astro-ph]].

[5] V. Springel, S. D. M. White, A. Jenkins, C. S. Frenk, N. Yoshida, L. Gao, J. Navarro and R. Thacker *et al.*, Nature **435** (2005) 629 [astro-ph/0504097].

[6] T. Buchert and J. Ehlers, Astron. Astrophys. **320** (1997) 1 [astro-ph/9510056].

[7] S. Räsänen, Phys. Rev. D **85** (2012) 083528 [arXiv:1107.1176 [astro-ph.CO]].

[8] I. A. Brown, J. Latta and A. Coley, Phys. Rev. D **87** (2013) 4, 043518 [arXiv:1211.0802 [gr-qc]].

[9] R. Maartens, Phil. Trans. Roy. Soc. Lond. A **369** (2011) 5115 [arXiv:1104.1300 [astro-ph.CO]].

[10] S. Nadathur, Mon. Not. Roy. Astron. Soc. **434** (2013) 398 [arXiv:1306.1700 [astro-ph.CO]].

[11] H. Bondi, Mon. Not. Roy. Astron. Soc. 107: 410, 1947.

[12] N. Mustapha, C. Hellaby and G. F. R. Ellis, Mon. Not. Roy. Astron. Soc. **292** (1997) 817 [gr-qc/9808079].

[13] K. Enqvist, Gen. Rel. Grav. **40** (2008) 451 [arXiv:0709.2044 [astro-ph]].

[14] J. Garcia-Bellido and T. Haugboelle, JCAP **0909** (2009) 028 [arXiv:0810.4939 [astro-ph]].

[15] J. Garcia-Bellido and T. Haugboelle, JCAP **0804** (2008) 003 [arXiv:0802.1523 [astro-ph]].

[16] S. Alexander, T. Biswas, A. Notari and D. Vaid, JCAP **0909** (2009) 025 [arXiv:0712.0370 [astro-ph]].

[17] T. Biswas, A. Notari and W. Valkenburg, JCAP **1011** (2010) 030 [arXiv:1007.3065 [astro-ph.CO]].

[18] V. Marra and A. Notari, Class. Quant. Grav. **28** (2011) 164004 [arXiv:1102.1015 [astro-ph.CO]].

[19] J. P. Zibin, A. Moss and D. Scott, Phys. Rev. Lett. **101** (2008) 251303 [arXiv:0809.3761 [astro-ph]].

[20] A. Moss, J. P. Zibin and D. Scott, Phys. Rev. D **83** (2011) 103515 [arXiv:1007.3725 [astro-ph.CO]].

[21] J. P. Zibin, Phys. Rev. D **84** (2011) 123508 [arXiv:1108.3068 [astro-ph.CO]].

[22] C. Clarkson and M. Regis, JCAP **1102** (2011) 013 [arXiv:1007.3443 [astro-ph.CO]].

[23] J. Garcia-Bellido and T. Haugboelle, JCAP **0809** (2008) 016 [arXiv:0807.1326 [astro-ph]].

[24] J. P. Zibin and A. Moss, Class. Quant. Grav. **28** (2011) 164005 [arXiv:1105.0909 [astro-ph.CO]].

[25] C. M. Yoo, K. i. Nakao and M. Sasaki, JCAP **1010** (2010) 011 [arXiv:1008.0469 [astro-ph.CO]].

[26] R. G. Clowes, L. E. Campusano, M. J. Graham and I. K. Soechting, arXiv:1108.6221 [astro-ph.CO].

[27] R. G. Clowes, K. A. Harris, S. Raghunathan, L. E. Campusano, I. K. Soechting and M. J. Graham, arXiv:1211.6256 [astro-ph.CO].

[28] J. Yadav, S. Bharadwaj, B. Pandey and T. R. Seshadri, Mon. Not. Roy. Astron. Soc. **364** (2005) 601 [astro-ph/0504315].

[29] K. T. Inoue and J. Silk, Astrophys. J. **648** (2006) 23 [astro-ph/0602478].

[30] W. Valkenburg, JCAP **1201** (2012) 047 [arXiv:1106.6042 [astro-ph.CO]].

[31] I. Szapudi, A. Kovcs, B. R. Granett, Z. Frei, J. Silk, W. Burgett, S. Cole and P. W. Draper *et al.*, arXiv:1405.1566 [astro-ph.CO].

[32] S. Nadathur, M. Lavinto, S. Hotchkiss and S. Rsnen, arXiv:1408.4720 [astro-ph.CO].

[33] T. Thiemann, Cambridge, UK: Cambridge Univ. Pr. (2007) 819 p [gr-qc/0110034].

[34] Arnowitt, R.; Deser, S.; Misner, C. W. Physical Review, vol. 116, Issue 5, pp. 1322-1330 (1959)

[35] Arnowitt, R.; Deser, S. Physical Review, vol. 113, Issue 2, pp. 745-750 (1959)

[36] R. L. Arnowitt, S. Deser and C. W. Misner, Gen. Rel. Grav. **40** (2008) 1997 [gr-qc/0405109].

[37] T. W. Baumgarte and S. L. Shapiro, Phys. Rev. D **59** (1999) 024007 [gr-qc/9810065].

[38] J. E. Lidsey, A. R. Liddle, E. W. Kolb, E. J. Copeland, T. Barreiro and M. Abney, Rev. Mod. Phys. **69** (1997) 373 [astro-ph/9508078].

[39] L. E. Parker and D. J. Toms, Quantum Field Theory in Curved Spacetime, Cambridge University Press (2009).

[40] V. Trimble, Ann. Rev. Astron. Astrophys. **25** (1987) 425.

[41] R. J. Gaitskell, Ann. Rev. Nucl. Part. Sci. **54** (2004) 315.

[42] T. Padmanabhan, AIP Conf. Proc. **843** (2006) 111 [astro-ph/0602117].

[43] T. Buchert, gr-qc/0001056.

[44] T. Buchert, Gen. Rel. Grav. **40** (2008) 467 [arXiv:0707.2153 [gr-qc]].

[45] J. Larena, J. –M. Alimi, T. Buchert, M. Kunz and P. -S. Corasaniti, Phys. Rev. D **79** (2009) 083011 [arXiv:0808.1161 [astro-ph]].

[46] L. Andersson and A. Coley, Class. Quant. Grav. **28** (2011) 160301.

[47] I. A. Brown, J. Behrend and K. A. Malik, JCAP **0911** (2009) 027 [arXiv:0903.3264 [gr-qc]].

[48] T. Kai, H. Kozaki, K. i. nakao, Y. Nambu and C. M. Yoo, Prog. Theor. Phys. **117** (2007) 229 [gr-qc/0605120].

[49] T. Biswas and A. Notari, JCAP **0806** (2008) 021 [astro-ph/0702555 [ASTRO-PH]].

[50] V. Marra, E. W. Kolb, S. Matarrese and A. Riotto, Phys. Rev. D **76** (2007) 123004 [arXiv:0708.3622 [astro-ph]].

[51] V. Marra, E. W. Kolb and S. Matarrese, Phys. Rev. D **77** (2008) 023003 [arXiv:0710.5505 [astro-ph]].

[52] K. Bolejko, Gen. Rel. Grav. **41** (2009) 1737 [arXiv:0804.1846 [astro-ph]].

[53] M. Lavinto, S. Räsänen and S. J. Szybka, JCAP **1312** (2013) 051 [arXiv:1308.6731 [astro-ph.CO]].

[54] B. D. Fields, Ann. Rev. Nucl. Part. Sci. **61** (2011) 47 [arXiv:1203.3551 [astro-ph.CO]].

[55] M. Regis and C. Clarkson, Gen. Rel. Grav. **44** (2012) 567 [arXiv:1003.1043 [astro-ph.CO]].

[56] P. J. E. Peebles and B. Ratra, Rev. Mod. Phys. **75** (2003) 559 [astro-ph/0207347].

[57] V. Sahni, Lect. Notes Phys. **653** (2004) 141 [astro-ph/0403324].

[58] M. Li, X. -D. Li, S. Wang and Y. Wang, Commun. Theor. Phys. **56** (2011) 525 [arXiv:1103.5870 [astro-ph.CO]].

[59] J. Einasto, Braz. J. Phys. **43** (2013) 369 [arXiv:1308.2534 [astro-ph.CO]].

[60] D. J. Schwarz, arXiv:1003.3026 [astro-ph.CO].

[61] W. L. Freedman *et al.* [HST Collaboration], Astrophys. J. **553**, 47 (2001). [arXiv:astro-ph/0012376].

[62] A. Sandage, G. A. Tammann, A. Saha, B. Reindl, F. D. Macchetto and N. Panagia, Astrophys. J. **653**, 843 (2006). [arXiv:astro-ph/0603647].

[63] A. G. Riess *et al.*, Astrophys. J. **699**, 539 (2009) [arXiv:0905.0695 [astro-ph.CO]].

[64] G. Efstathiou, arXiv:1311.3461 [astro-ph.CO].

[65] W. L. Freedman and B. F. Madore, Astrophys. **48** (2010) 673 [arXiv:1004.1856 [astro-ph.CO]].

[66] R. Tripp and D. Branch, Astrophys. J. **525** (1999) 209 [astro-ph/9904347].

[67] P. A. R. Ade *et al.* [BICEP2 Collaboration], arXiv:1403.3985 [astro-ph.CO].

[68] B. Audren, D. G. Figueroa and T. Tram, arXiv:1405.1390 [astro-ph.CO].

[69] N. Suzuki, D. Rubin, C. Lidman, G. Aldering, R. Amanullah, K. Barbary, L. F. Barrientos and J. Botyanszki *et al.*, Astrophys. J. **746** (2012) 85 [arXiv:1105.3470 [astro-ph.CO]].

[70] R. Amanullah *et al.*, Astrophys. J. **716**, 712 (2010) [arXiv:1004.1711 [astro-ph.CO]].

[71] P. Zhang and A. Stebbins, Phys. Rev. Lett. **107** (2011) 041301 [arXiv:1009.3967 [astro-ph.CO]].

[72] S. Flender, S. Hotchkiss and S. Nadathur, JCAP **1302** (2013) 013 [JCAP **1302** (2013) 013] [arXiv:1212.0776 [astro-ph.CO]].

[73] B. R. Granett, M. C. Neyrinck and I. Szapudi, Astrophys. J. **683** (2008) L99 [arXiv:0805.3695 [astro-ph]].

[74] D. J. Eisenstein and W. Hu, Astrophys. J. **496** (1998) 605 [astro-ph/9709112].

[75] D. J. Eisenstein *et al.* [SDSS Collaboration], Astrophys. J. **633** (2005) 560 [astro-ph/0501171].

[76] W. J. Percival, S. Cole, D. J. Eisenstein, R. C. Nichol, J. A. Peacock, A. C. Pope and A. S. Szalay, Mon. Not. Roy. Astron. Soc. **381** (2007) 1053 [arXiv:0705.3323 [astro-ph]].

[77] A. Cabre and E. Gaztanaga, arXiv:1011.2729 [astro-ph.CO].

[78] V. Springel, C. S. Frenk and S. D. M. White, Nature **440** (2006) 1137 [astro-ph/0604561].

[79] A. G. Lemaître, LUnivers en expansion, Annales de la Socie'te' Scientifque de Bruxelles A53, 51 (1933).

[80] K. Bolejko, Mon. Not. Roy. Astron. Soc. **370** (2006) 924 [astro-ph/0503356].

[81] K. Bolejko and P. Lasky, arXiv:0809.0334 [astro-ph].

[82] A. A. H. Alfedeel, C. Hellaby, Gen. Rel. Grav. **42**, 1935-1952 (2010) [arXiv:0906.2343 [gr-qc]].

[83] M. E. Cahill, G. C. McVittie, J. Math. Phys. **11**, 1382 (1970).

[84] M. E. Cahill, G. C. McVittie, J. Math. Phys. **11**, 1392 (1970).

[85] J. P. Zibin, Phys. Rev. D **78** (2008) 043504 [arXiv:0804.1787 [astro-ph]].

[86] K. Van Acoleyen, JCAP **0810** (2008) 028 [arXiv:0808.3554 [gr-qc]].

[87] W. C. Lim, M. Regis and C. Clarkson, JCAP **1310** (2013) 010 [arXiv:1308.0902 [astro-ph.CO]].

[88] W. Valkenburg, V. Marra and C. Clarkson, Mon. Not. Roy. Astron. Soc. **438** (2014) L6 [arXiv:1209.4078 [astro-ph.CO]].

[89] A. E. Romano, M. Sasaki and A. A. Starobinsky, Eur. Phys. J. C **72** (2012) 2242 [arXiv:1006.4735 [astro-ph.CO]].

[90] B. Sinclair, T. M. Davis and T. Haugbolle, Astrophys. J. **718** (2010) 1445 [arXiv:1006.0911 [astro-ph.CO]].

[91] W. Valkenburg, Gen. Rel. Grav. **44** (2012) 2449 [arXiv:1104.1082 [gr-qc]].

[92] M. Doran and M. Lilley, Mon. Not. Roy. Astron. Soc. **330** (2002) 965 [astro-ph/0104486].

[93] E. Komatsu *et al.* [WMAP Collaboration], Astrophys. J. Suppl. **192** (2011) 18 [arXiv:1001.4538 [astro-ph.CO]].